Title
Automated approaches for extracting individual tree level forest information using high spatial resolution remotely sensed data

Author
Lee, Jun Hak

Publication Date
2010

Peer reviewed|Thesis/dissertation

Automated approaches for extracting individual tree level forest information using high spatial resolution remotely sensed data

by

Jun Hak Lee

A dissertation submitted in partial satisfaction of the

requirements for the degree of

Doctor of Philosophy

in

Environmental Science, Policy and Management

in the

Graduate Division

of the

University of California, Berkeley

Committee in charge:

Professor Gregory S. Biging, Chair
Professor Peng Gong
Professor John Radke

Fall 2010

Abstract

Automated approaches for extracting individual tree level forest information using high spatial resolution remotely sensed data

by

Jun Hak Lee

Doctor of Philosophy in Environmental Science, Policy, and Management
University of California, Berkeley

Professor Gregory S. Biging, Chair

Detailed forest information is increasingly desired not only for forest management purposes but also for maintaining and enhancing sustainable forest ecosystems. Although precise measurements of forests can be gathered by field measurements, they are labor intensive and time consuming especially when obtaining enough measurements over large and heterogeneous forest areas. Therefore we need automated and accurate methods which can supplement field measurements. High spatial resolution remotely sensed data can be applied for this objective because developing technologies keep increasing spatial resolution and make it possible to handle large amounts of remotely sensed digital data by powerful computers at reasonable prices. Although high spatial resolution remotely sensed data holds the potential to be a valuable source of information for forest characteristics, a number of challenges still exist in extracting the desired information from this data. Therefore, it is critical to develop and improve automated methods to extract forest information. In this dissertation, I develop and improve the automated methods of extracting individual tree level forest biophysical parameters using high spatial resolution remotely sensed data. While there are many new remote sensing technologies, such as digital aerial photographs, LiDAR (Light Detection and Ranging), radar, and multispectral (or hyperspectral) data, I mainly focus on small footprint LiDAR and aerial images (by digital frame camera) in this study, because these sensors can provide very high spatial resolution data, which are necessary to extract individual tree level biophysical characteristics.

This study consists of three parts, which are basic procedures to exploit high spatial remotely sensed data to extract individual tree level forest biophysical parameters. All three studies are conducted in a mixed-conifer forest at Angelo Coast Range Reserve on the South Fork of the Eel River in Mendocino County, California, USA. First, I develop a robust method to reconstruct Digital Terrain Model (DTM) by classifying raw LiDAR points into ground and non-ground points with the Progressive Terrain Fragmentation (PTF) method. PTF applies iterative steps for searching terrain points by approximating terrain surfaces using the TIN (Triangulated Irregular Network) model constructed from the ground return points. Instead of using absolute slope or offset distance, the proposed method utilizes orthogonal distance to and relative angle between a triangular plane and a node. For that reason, PTF was able to classify raw LiDAR points into ground and non-ground points on a heterogeneous steep forested area with a small number of parameters. The results show the robust performance of the proposed method even under complex terrain conditions. Second, I develop an automated method to detect individual

tree tops and delineate individual tree-crown boundaries using airborne LiDAR data. Because of heterogeneous site conditions, I divide the study site into two height classes (high and low trees). For high trees (>= 25 m), I detect tree tops by using a progressive window-size local maximum filter and I conduct an additional verification procedure to reduce false tree top detection by using the shape of canopy profiles between trees. Then, I delineate tree-crown boundaries by marker-controlled watershed segmentation. For low trees (< 25 m), I apply a fixed window-size local maximum filter (1 m radius) to detect tree tops, and I apply the skeleton by influence zones (SKIZ) segmentation to delineate crown boundaries. Compared to fixed window-size local maximum filtering method, our method performed better for detecting and delineating individual trees regardless of tree sizes. Third, I combine aerial images and LiDAR data by means of automated registration procedures using tree tops as corresponding control points. A morphological operation (extended-maxima transformation) is applied to detect tree tops (as common control points) from aerial images and LiDAR data. I conduct the preliminary matching by using the small region of the image center, which was near the principal point. Then, I iteratively expand the control points to the entire images by using the backward projection of the tree top points of the LiDAR data over the aerial images. I employ a local transformation method (piecewise linear transformation) by using detected control points. The adjacent geo-rectified images are mosaicked into one large image by using the seam lines, which are created from the common control points between images. The result shows that the proposed approach enables us to register aerial images with airborne LiDAR data by using individual trees as common control points.

In this study, I develop and improve the automated approaches for extracting individual tree level forest information with high spatial resolution remotely sensed data. I expect the proposed approaches may contribute to cope with a number of challenges for forest information extraction from high spatial resolution remotely sensed data.

Table of Contents

List of Figures

List of Tables

Acknowledgements

First of all, I would like to express my deepest gratitude to Professor Greg Biging for his guidance and support throughout the years I have been in Berkeley. Without his insightful supervision, I would not have been able to complete this dissertation. At all times of my research, he guided me with trust and patience which enabled me to develop my problem solving ability during the PhD program. Furthermore, his stimulating suggestions and encouragement made me keep pursuing my research with patience to overcome challenges. I feel so fortunate to have him as my advisor.

I also would like to thank Professor Peng Gong. His scholarly knowledge in remote sensing inspired me to research advanced remote sensing methods in ecosystem science. Also, his outstanding insights in his extensive studies provided a foundation for my doctoral research. I also wish to give my special thanks to Professor John Radke, who has shown enormous interests in my ideas and has been particularly supportive of my research. His brilliant ideas in spatial analysis strongly motivated me to explore various techniques in Geographic Information System (GIS). Our common interests and vision for future GIS applications for societies facilitated me to enjoy my research with confidence. I would like to extend my thanks to Professors John Battles, Maggi Kelly, Kevin O'Hara, and Dennis Baldocchi for their scholarly advice and thoughtful comments on my research.

I am indebted to Professor Bill Dietrich and the National Center of Airborne Laser Mapping (NCALM) for generously allowing me to use the essential data sets (LiDAR - Light Detection and Ranging) for my study.

I am obliged to Professor David Ragland for providing me an opportunity to extend my skill of spatial data analysis to a wide range of disciplines from ecosystem modeling to public health applications.

I would like to express my special appreciation to Professor Woo-Kyun Lee of Korea University, who guided and enabled me to pursue a doctoral degree at UC Berkeley. I also thank Dr Seong-Woo Jeon of Korea Environment Institute (KEI), who gave me a chance to work on a granted research with KEI.

I cannot forget to thank Josh Fisher, who was a lab mate, a workout partner, and my best friend from the beginning of my life in Berkeley. I would like to extend my gratitude to my research group members, who have shared various research interests: Qi Chen, Desheng Liu, Qinghua Guo, Qian Yu, Alan Di Vittorio, Tim Robards, Ashley Holts, Josh Harmsen, Liheng Zhong, John Dingman, Kyle Holland, Iryna Dronova, and Yu-Ting Huang. I thank Tammy Spath and Jeff Caldwell for their help in improving my writing skills.

As always, I am grateful to my family for their unconditional love and care throughout my life. Also, I thank the Wilkinson family in Berkeley, who have taken care of me as though I were a member of their family. Last but not least, I devote my greatest gratitude to my wife, Yekang Ko, who is with me and will be with me through thick and thin.

Chapter 1 Introduction

1.1 Background

Forests, as major components of land surface, play important roles in sustaining the Earth's ecosystems. However, forested areas have rapidly decreased because of the demand for resources and land use by population growth (Franklin, 2001). In addition, decreasing forest areas and increasing fossil fuel consumption have been altering global climate (Houghton et al., 2001). Forest disturbances are increasingly caused by climate change and these disturbances threaten the sustainability of forest ecosystems (Millar et al., 2007; Dale et al., 2001). Because forests are complex and characterized by multiple-scale structure and dynamical patterns, continuous and precise monitoring and assessments of large forest areas are critically required (Lamonaca et al., 2008). Although precise measurements of individual trees can be gathered by field measurements, field measurements are labor intensive and time consuming especially when obtaining enough measurements over large and heterogeneous forest areas. In addition, a data collection approach using field measurements provides only a narrow window of the entire area, so that it is difficult to depict the heterogeneity and complexity of the system by using only field measurements. Therefore, we need automated and accurate methods which can supplement field measurements. High spatial resolution remotely sensed data can be applied for this objective because developing technologies keep increasing spatial resolution and make it possible to handle large amounts of remotely sensed digital data by powerful computers at reasonable prices.

Interpretation of the term "high spatial resolution" (or "low spatial resolution") is subjective and mainly depends on the field of application and the feature of interest. Strahler et al. (1986) mention that spatial resolution can be determined by the size of the object that we desire to sense. In the low resolution case, the resolution cells of the image are larger than the objects of interest. On the other hand, the resolution cells of the image are smaller than the objects of interest in the high resolution case (Strahler et al., 1986). Therefore, high spatial resolution images contain multiple pixels for each object. Because the object of our interest is an individual tree, which is a fundamental structural element in forests, high spatial resolution refers to images whose pixel dimensions are less than or equal to 1 m (Culvenor, 2003; Wang, 2003).

While we have many new remote sensing technologies, such as digital aerial photographs, LiDAR (Light Detection and Ranging), radar, and multispectral (or hyperspectral) data, proper automated processing methods, which can detect individual trees in the forests, still need further development (Brandtberg, 1999). In this study, we mainly focus on small footprint LiDAR and aerial images (from a digital frame camera) because these sensors can provide very high spatial resolution data, which are necessary to extract individual tree level biophysical characteristics.

1.2 High spatial resolution remote sensing data

LiDAR (Light Detection and Ranging)

Among the various remote sensing methods, discrete-return, small-footprint LiDAR systems are highly effective in extracting detailed forest biophysical parameters, because LiDAR can provide detailed 3-dimentional surfaces (both canopy and ground) data with high spatial resolution and accuracy (Lim et al., 2003; Reutebuch et al., 2005). The basic measurement made by LiDAR is the range between the sensor and a target surface. The range is determined by the elapsed time between the emissions of a short-duration laser pulse and the arrival of the reflection of that pulse in the sensor. Based on our knowledge of the speed of light, the elapsed time is converted

to the distance between the sensor and a target surface (Lefsky et al., 2002; Wulder et al., 2008). The precise sensor location is obtained by a Differential Global Positioning System (DGPS) and the orientation is acquired from an Inertial Navigation System (INS). Based on this information, every laser pulse can be automatically geo-registered with vertical and horizontal accuracies of approximately 15 and 40 cm, respectively (Davenport et al., 2004). Because discrete-return LiDAR systems have a small diameter of footprint (0.1 to 2 m) and high repetition pulse rates, we can obtain very high spatial resolution data with dense sampling points (Lim et al., 2003; Lefsky et al., 2002). The high density of laser pulses enables us to observe individual tree crowns from a cloud of LiDAR points (Wulder et al., 2008). Subsequently, there are a growing number of attempts to detect individual trees and to extract individual tree attributes (such as tree height, timber volume, and forest biomass) over extensive forested areas by using discrete-return LiDAR (Jensen et al., 2006; Lee and Lucas, 2007; Naesset et al., 2004; Popescu, 2007; Wulder et al., 2008).

Aerial photography (digital aerial images)

Aerial photographs (and digital aerial images) have widely used as a tool for monitoring and managing forest resources mainly because we can acquire very high spatial resolution images with large geographic extent at reasonable cost. The geographic extent, resolution and cost of imagery have made this type of imagery more widely used than any other data source. (Hall, 2003; Fensham and Fairfax, 2002). Traditionally, the extraction of forest inventory parameters was conducted by a visual interpretation method (Yu, 2007). However an increasing number of automated approaches have been proposed to extract features that represent detailed forest structural characteristics (Hall, 2003). Aerial photographs provide geometrically and radiometrically high quality images with multispectral capability (Baltsavias, 1999). In addition, aerial photographs span a greater time than other remote sensing data so that aerial photographs have been used for retrospective analysis of forest ecosystem dynamics (Fensham and Fairfax, 2002; Vega and St-Onge, 2008; Kadmon and Harari-Kremer, 1999).

1.3 Motivation

With growing demands for detailed forest information, high spatial resolution remotely sensed data is receiving more attention as a valuable source of information. However, automation of image (data) analysis procedures is essential to utilize the full potential of high spatial resolution data, due to the volume and complexity of the data, which make it almost impossible to apply manual interpretation methods to extract forest inventory information from extensive forested areas. Therefore, it is critical to develop and improve automated methods to extract forest inventory information from high spatial resolution data. Although the continuously improving spatial resolution of the sensors provide a rapidly growing amount of data, the higher spatial resolution does not directly improve the quality and context of forest inventory information due to the fact that each pixel describes just a part of the object of interest (individual tree crown) and cannot fully represent the object. To overcome this limitation, we need an alternative approach, which recognizes and extracts meaningful objects from the remotely sensed data (e.g. individual trees as a fundamental structural element in forests). Accordingly, it is critical to improve automated methods to recognize individual trees and extract forest inventory parameters from high spatial resolution data. Although extensive attempts have been made to extract information from the data sets, there are strong demands for continuing development and improvement of the automated interpretation methods. Therefore, it is necessary to improve a method to detect and

recognize individual trees from the data sets (Koch and Dees, 2008; Koch et al., 2006). In addition, a robust method to reconstruct ground surface information needs to be developed and improved so that ground surface information can be employed to extract the vertical structure of forested areas (Liu, 2008). Regardless of sensor type, more and more data are acquired from different sources. Consequently, integrated analysis of spatial data has become increasingly important. In particular, an integration of multisource high spatial resolution data is difficult because of the high demand for the geometric accuracy, and the high variances and complexities of the data sets. As a critical prerequisite to fully utilize the advantages of multisource remote sensing data, we also need a new approach to integrate high spatial resolution multiple data sources (Habib et al., 2005; Schenk and Csathó, 2002)

1.4 Objectives of the dissertation

The objective of this dissertation is to develop an automated method of extracting individual tree level biophysical parameters using high spatial resolution remotely sensed data. I am focusing on developing and evaluating new approaches which are essential for using high spatial resolution data (discrete-return LiDAR and digital aerial images) in forest ecosystem applications. More specifically, I intend to achieve three objectives through my dissertation:

1. To develop a robust method that classifies raw LiDAR points into ground and non-ground points by using a progressive terrain fragmentation method, which iteratively densifies a triangular surface by relatively robust criteria.

2. To develop a method to detect tree tops and delineate an individual tree crown with a LiDAR driven digital surface model as well as with raw LiDAR point clouds.

3. To combine aerial images and LiDAR data by means of automated registration procedures using tree tops as corresponding control points.

1.5 Organization of the dissertation

The dissertation consists of five chapters and is arranged as follows:

Chapter 1 discusses the background and motivation of this research, and introduces the objectives and organization of the dissertation.

Chapter 2 describes a new approach to reconstruct DTM (Digital Terrain Model) from discrete-return raw LiDAR points. I propose the Progressive Terrain Fragmentation (PTF) method, which applies iterative procedures for searching terrain points by approximating terrain surfaces using the TIN (Triangulated Irregular Network) model constructed from the ground return points which are classified from the previous steps.

Chapter 3 illustrates a new method for detecting and delineating individual trees in structurally heterogeneous forests using airborne LiDAR data. In this chapter, I describe the proposed method which employs a progressive filter size to detect tree tops from the raw LiDAR points and uses a DSM (Digital Surface Model) to delineate canopy boundaries.

Chapter 4 focuses on an individual tree-based automatic registration of aerial images with airborne LiDAR data. In this chapter, I introduce an automated approach to extract feature points (tree tops) from the aerial images and the LiDAR data and to find corresponding pairs to improve the accuracy of image registration.

Chapter 5 concludes the dissertation work and discusses future developments

Chapter 2 Classifying Discrete Return LiDAR Data for Generating Terrain Model in Forested Environment Using Progressive Terrain Fragmentation Method

2.1 Introduction

Using airborne light detection and ranging (LiDAR) for topographic mapping is rapidly becoming a standard practice in geo-spatial science because LiDAR system is one of the most effective methods of extracting three-dimensional shapes of a terrestrial environment (Hodgson and Bresnahan, 2004; Liu, 2008). LiDAR expands its attractiveness in various types of applications such as hydrological modeling, coastal management, urban planning, landscape ecology, and forest management (Lefsky et al., 2002; Lim et al., 2003; Wulder et al., 2008)

Compared to traditional remote sensing techniques, LiDAR provides both horizontal and vertical information (Lim et al., 2003). Therefore, LiDAR is one of the most effective methods for quantitative assessment of forest parameters because it is able to directly depict 3D object shapes by capturing high density and high accuracy three-dimensional point clouds in object space (Habib et al., 2005). Because the LiDAR signal has the ability to pass through gaps in foliage and reflect from different parts of a forest canopy, several studies used LiDAR data for extracting forest biophysical parameters (such as tree height, timber volume, and forest biomass) over extensive forested areas (Jensen et al., 2006; Lee and Lucas, 2007; Naesset et al., 2004; Popescu, 2007; Wulder et al., 2008). Forest measurement by airborne laser scanning requires a DTM (digital terrain model) for representing the ground surface and a DSM (digital surface model) for describing the canopy surface (Hyyppä et al., 2008). Thus, creating an accurate terrain surface is critical for accurate forest parameter estimation because an incorrect terrain surface model causes propagational errors in forest parameter estimation.

Even though airborne laser scanning provides highly accurate 3D point clouds representing surface shapes in great detail, there is no distinction in raw LiDAR points whether a point represents a terrain or non-terrain object. It is a prerequisite to separate clouds of LiDAR points into ground returns and non-ground returns in almost all of the applications using airborne laser scanning (Evans and Hudak, 2007). Accordingly, efficient and accurate ground filtering is critical in using airborne laser scanning across disciplines as well as in forest applications. Although terrain surface extraction is an essential part of processing LiDAR data, it is surprisingly difficult to extract accurate terrain surface from raw LiDAR point clouds and there is a broad range of studies for extracting bare earth surface from LiDAR data (Liu, 2008).

Sithole and Vosselman (2004) used four categories including slope-based, block-minimum, surface-based, and clustering/segmentation methods and discussed characteristics of each approach. Liu (2008) used slightly different categories to review several research studies and addressed interpolation-based, slope-based, and morphological methods as the most popular approaches.

The slope-based method developed by Vosselman (2000) used an assumption that the gradient of natural ground slope is distinctly different from the slope of non-ground objects such as trees and buildings to separate ground and non-ground points (Sithole and Vosselman, 2001). Vosselman's method is only applicable for gently sloped areas because a single static gradient threshold failed to distinguish terrain slope vs. non-terrain object when the terrain has steep slopes. Sithole and Vosselman (2001) modified previous methods so that the threshold changes with the terrain slopes. However, this method still has limited filtering performance in areas with large buildings or low vegetation penetration.

Interpolation-based methods, first proposed by Kraus and Pfeifer (1998), iteratively approximate the ground using weighted linear least squares interpolation. This method creates a rough approximation of the terrain surface and uses it to calculate residuals (offset between the points and the surface). Based on calculated residual, different weights are assigned to each point. Points of negative residual are more likely to be ground points than the others so that more weight is assigned for points of negative residuals to calculate terrain interpolation. Lee and Younan (2003) enhanced Kraus and Pfeifer's method by implementing adaptive line enhancement (ALE) - substituting the least squares method with normalized least squares so that it creates a robust terrain surface even for steep slopes or spurious peaks. However, the ALE method needs a number of parameters (delay factor and adaptation parameters) and relatively subjective trial and error procedures are still required to select appropriate parameters.

Morphological methods exploit morphological operators (mainly opening) to remove non-terrain objects. Morphological methods are relatively simple and fast so that they have an advantage in processing large amounts of LiDAR points. Defining optimal operator size is the key factor in creating a correct terrain surface; removing non-ground objects, yet keeping the shape of the terrain surface. However, it is almost impossible to meet this demand with one fixed window size. Kilian et al. (1996) applied the morphological operator (opening) several times with different operator sizes starting from the smallest window size. Then each point was assigned different weights proportional to the window size when it is classified as a ground point. Zhang et al. (2003) suggested progressive use of morphological filters to remove non-ground features by gradually increasing the window size of the filter and the thresholds were determined by the elevation difference between surfaces before and after filtering. This method assumed the slope is constant. However, the major limitation of this method is that a constant slope over the area is not a realistic condition especially in complex environments. Chen et al. (2007) improved the method of Zhang et al. (2003) in that their method does not require the assumption of a constant slope. They used the fact that non-terrain objects (such as buildings) normally have sudden elevation changes along the edges but the change of ground is usually not abrupt like non-terrain objects. This method showed encouraging results compared to other methods with minimum required parameters and assumptions. In general, this method performs well but when LiDAR points do not have enough penetration through vegetation (such as in old and densely forested areas), this method can create false flat terrain surfaces under large trees in steep terrain areas.

The block-minimum (or local minimum) method is relatively simple. This method searches the minimum value from the neighbor points within a given spatial extent. (Clark et al., 2004; Cobby et al., 2001; Suarez et al., 2005). Even though the idea is simple, it is almost impossible to find one filter size that removes all non-terrain objects without compromising details of the terrain surface. Wack and Wimmer (2002) used an improved block-minimum method by implementing a hierarchical approach to detect non-ground raster elements.

Regardless of types of filtering methods, it is challenging to distinguish between ground returns and points reflected in the vegetation, where there is steep slope under dense forest cover (Kobler et al., 2007). This is because this type of area has sparse and spatially heterogeneous ground returns. In addition, due to a steep gradient of this type of area, slope based threshold methods do not work properly (Sithole and Vosselman, 2001). As raw LiDAR point data are normally processed in automated approaches due to large amounts of data, it is required to optimize filtering parameters with minimal user intervention (Kobler et al., 2007). Most existing filtering methods are based on the assumption that variations of natural terrain are more gradual than those of non-terrain surfaces. So, the majority of filtering methods calculate elevation differences and slopes changes and determine certain threshold values for distinct points (Meng et al., 2009; Sithole and Vosselman, 2004). Thus, it is necessary to gain prior knowledge of the sites to select threshold or parameter values. In addition, this assumption has shown limited success on steep and densely forested areas where the basic assumption breaks often because of steep terrain gradients and sparse ground points.

The objective of this study is to develop a robust method that classifies raw LiDAR points into ground and non-ground points by using a progressive terrain fragmentation method, which iteratively densifies a triangular surface by relatively robust criteria. This method is similar to Axelsson (2000)'s method. The unique point of our method is prioritizing a set of LiDAR points, which are used to approximate a triangulated irregular network (TIN) surface, so that important terrain points are added earlier than the other points in conjunction with minimizing to incorrectly include non-ground points during the iteration process.

2.2 Materials and methods

2.2.1 Progressive Terrain Fragmentation (PTF) Algorithm

The characteristics of TIN structure, which represents a surface as a set of non-overlapping contiguous triangular facets of irregular shape and size, are very effective in identifying subgroups of surfaces to represent heterogeneous terrain surfaces (Lee, 1991). The seed point set is used to generate the initial terrain surface in TIN structure and additional terrain points are included at the end of each iteration for the following terrain estimation. The key factor in this method is to set up criteria to select correct terrain points. It is challenging to set up criteria to filter out non-terrain points from the raw LiDAR point cloud for a large area of varied terrain characteristics. Even though there are extensive research studies for extracting the terrain surface model from raw LiDAR points, there is much room for improving efficiency and

accuracy of filtering methods with minimum user intervention (Liu, 2008; Silvan-Cardenas and Wang, 2006).

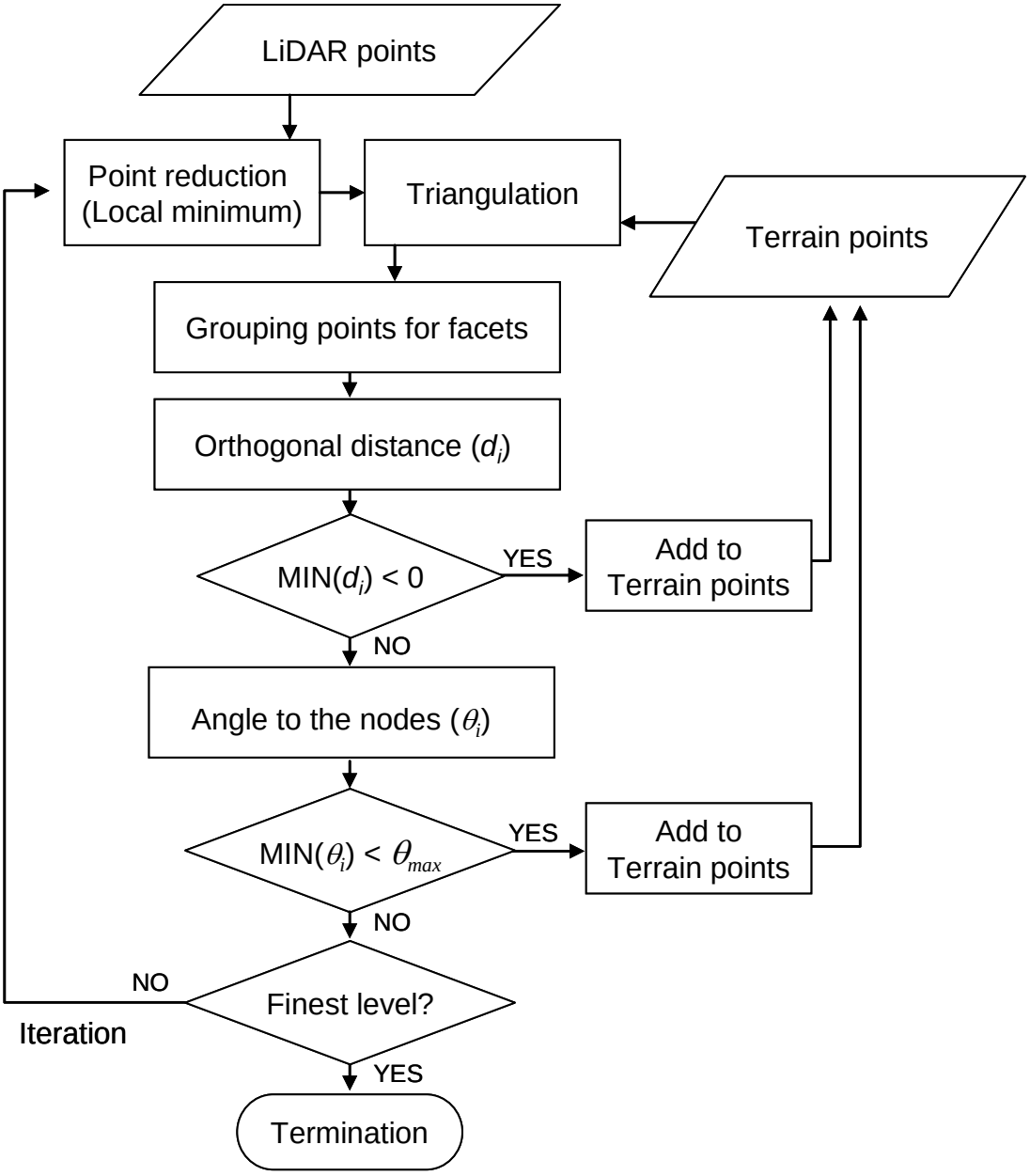

Figure 2-1. The flowchart of progressive terrain fragmentation algorithm.

In this study, first, multi-level local minimum point sets are prepared as candidate ground points from all raw LiDAR point clouds. From sparse point sets, the terrain approximation surface is estimated in TIN structure. Then, the points are added to TIN estimation in each iteration if the point satisfies certain criteria. The criteria differ by characteristics of each triangular surface in order to give priority to more important (or significant) points to approximate the terrain surface, yet minimize commission errors, where a non-ground point is incorrectly selected as a ground point. It is similar to Sohn and Dowman (2008)'s approach to classify TIN surfaces based on the characteristics of contained points. In our research, we classify TIN facet into convex and concave surfaces based upon the orthogonal distance between the facet and points as follows. The orthogonal distance between the TIN facet and candidate points are calculated. Then, if there is at least one negative point in the member points, the surface is classified as a "concave surface". For concave surfaces (downward surface), the point with maximum distance in the negative direction from the facet surface is selected and added to terrain points. Otherwise, if there are only positive offset points, it is classified as a "convex surface". For convex surfaces (upward surface), the point with the minimum angle (between a facet and a node point) within a certain threshold is selected. Then the selected point is added into the set of ground points for the next iteration. The flowchart of progressive terrain fragmentation algorithm is illustrated in Figure 2-1.

2.2.1.1. LiDAR points reduction

One of the most beneficial characteristics of LiDAR data is the ability to acquire high spatial data density with unprecedented detail by a 3D point cloud. On one hand, extremely high sampling point density makes it possible to extract a broad range of useful information from the data sets. On the other hand, a large volume of data requires a lot of storage resource and processing power. The iterative process especially requires extensive processing time and power. In optimal conditions, higher LiDAR point density (sampling density) can provide more accurate surface description. However, because only a small part of all data points is returned from terrain surfaces (especially heterogeneous forested areas), processing all raw LiDAR data pulses would be inefficient when there is no accuracy improvement for retrieving terrain elevation models (Liu, 2008).

In this research, we started with coarse data point density and increased data point density in the iteration processes. The approach used by this study is similar to the progressive TIN densification method (Axelsson, 2000) and recursive terrain fragmentation (Sohn and Dowman, 2008). These methods use a coarse-to-fine strategy, which starts with sparse points for an initial surface estimation and increases point density for fitting a real terrain surface by fragmenting triangular surfaces. Although only a small fraction of LiDAR points are selected and used for approximating the terrain surface at a coarse level of estimation, if all raw LiDAR points are used for the search process, it significantly drags down the efficiency of the process. In order to cope with this problem, multi level point sets are generated so that reduced point sets are used for

coarse scale stage and the next level of point sets (higher density) are used as the iteration continues.

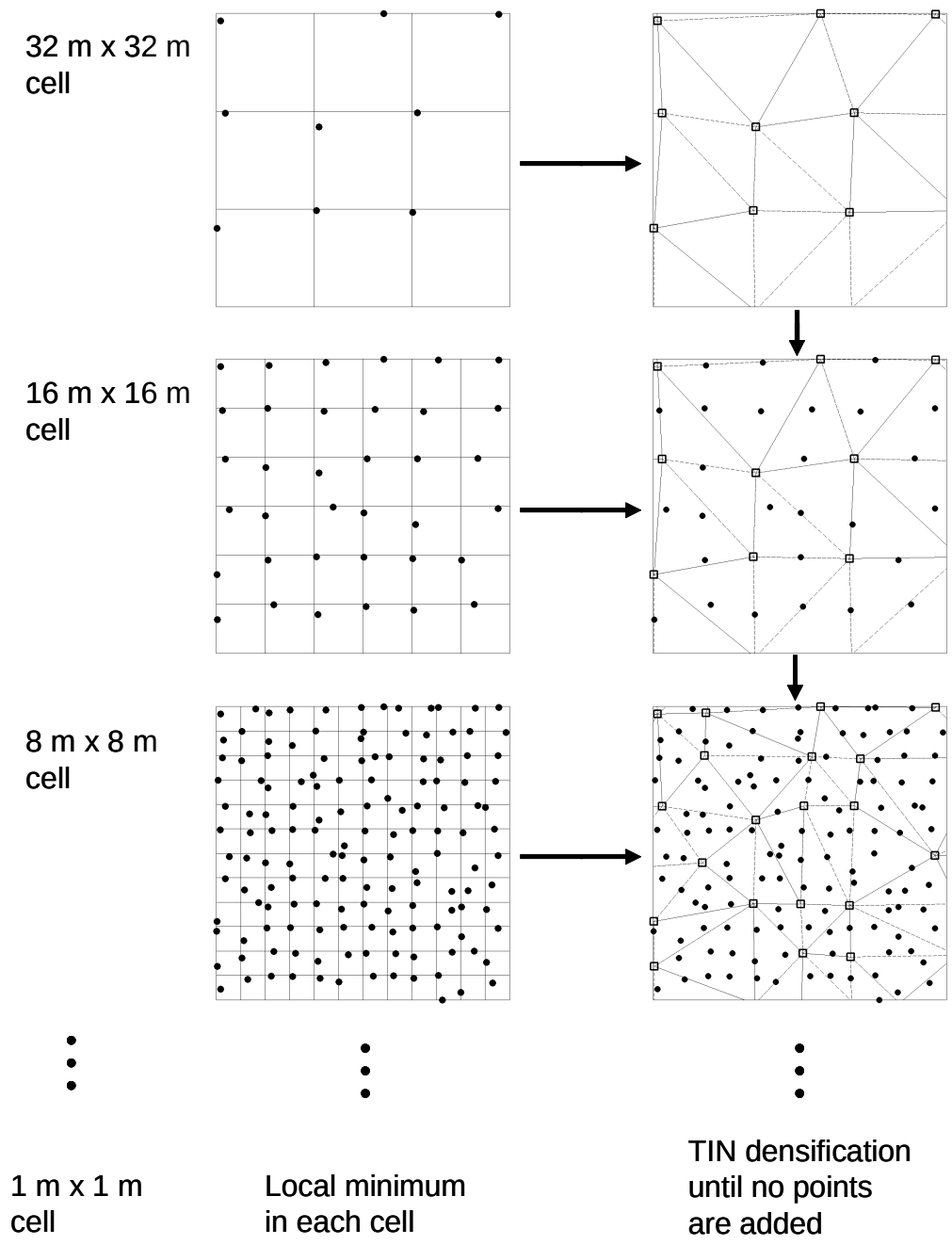

Figure 2-2. Example of LiDAR points reduction at different level and TIN surface fragmentation

Local minimum elevation points are selected as candidate terrain points in the hierarchical configuration that follows. A non-overlapping grid with squared cells is superimposed over the original raw LiDAR points. The minimum elevation value within each cell was selected as a candidate ground point. It started from a 1m x 1m sized cell and the size is doubled at each grid level until it reaches the maximum cell size, which could vary by user's decision. The maximum cell size is selected based on the largest type of structure in the area (Axelsson, 2000). In this study, 32 m is selected for the maximum cell size because 32 m is large enough to filter out the largest type of object (i.e. trees). Even though the surface fragmentation process is performed from coarse to fine scale, searching for the minimum value at each level is carried out in reverse scale (fine to coarse level) because the minimum point at a certain level is one of four minimum values of the previous level. For this reason, the number of points for searching for minimum elevation is decreased by 1/4 of the previous level and it is exponentially decreased throughout levels (Figure 2-2).

2.2.1.2. Triangulation and assign point for each facet

An initial TIN surface is derived from the coarsest level of the point sets with a grid size of *L1* (32 m). After that, the next level of point sets (extracted from a grid size of *L2* (16 m)), falling into the same facet, are grouped and the points of each group are processed separately with their own set of plane parameters from the facet where the points belong. Instead of calculating all the LiDAR points in each iteration step, coarse to fine scale level of point sets are used. Figure 2-2 illustrates triangulation from the set of reduced LiDAR points.

2.2.1.3. Searching terrain points

We calculated the orthogonal distance between all the member points, which falls into a certain triangle, and the triangle plane. Each triangle is defined by three nodes (terrain points selected from previous approximation) so that each planar surface is modeled from those three points. Initially, the planar equation is derived from three points. The orthogonal distance is calculated for each member point. Then, the characteristic of each triangle is classified as either a concave (downward) or convex (upward) plane as follows:

Concave: If there is at least one negative offset point in a facet, it is classified as a concave facet (Figure 2-3a). Then, a point, which has the minimum offset height (maximum distance in a negative direction from the facet), is searched within a specific facet and the selected point is added to the terrain point set (Figure 2-3b). These points, classified as terrain points, are used for creating the new surface at the next iteration.

Convex: A facet with no negative offset point is classified as a convex surface (Figure 2-3c). In this case, the minimum divergent point within a threshold angle is selected as a terrain point. For searching the minimum divergent point, we calculated angles between the node and the facet. There are three angles between a node and a TIN facet (tetrahedral shape) and the maximum

angle out of three is assigned to the node (as a representing angle) and used for assessing whether it is a ground or non-ground point in the filtering procedure (Figure 2-3d). The purpose of using the minimum divergent angle for concave surfaces is to minimize the possibility of commission errors (classifying non-ground point as ground points incorrectly). In this iterative procedure, commission errors could lead to serious propagational errors because falsely created terrain surfaces are used as a basis for the following raw point assessment.

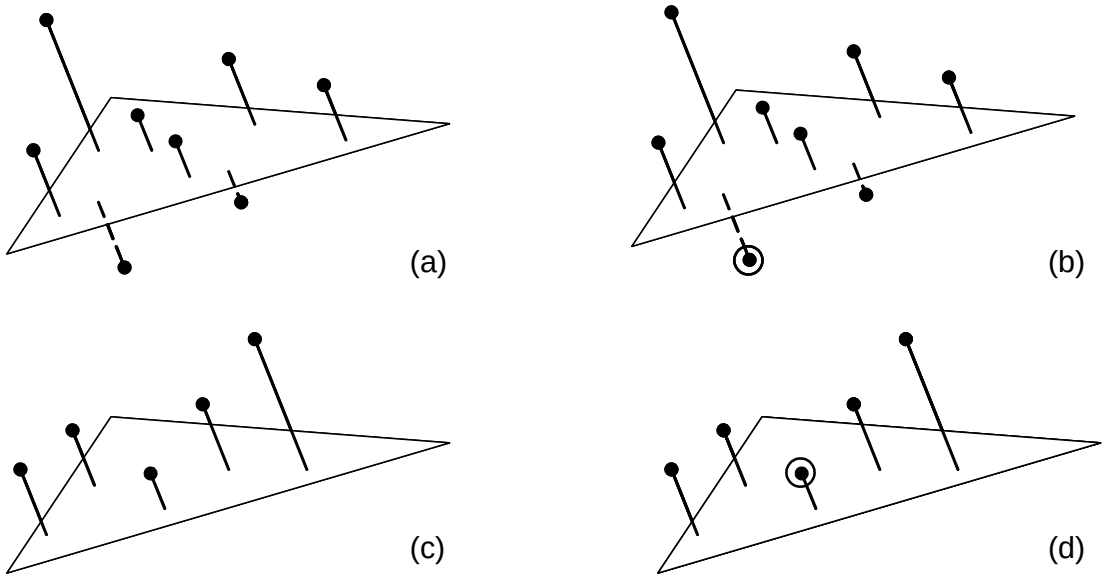

Figure 2-3. Illustration of triangular surface types and searching terrain points. (a) concave surface (b) selecting the maximum distance offset point in negative direction (c) convex surface (d) searching the minimum angle point within admissible angle range.

2.2.1.4. LiDAR points classification

It is common to interpolate raw LiDAR points into raster images before applying filtering procedures because filtering on raster images runs faster than processing raw LiDAR point clouds (Chen et al., 2007; Liu, 2008). However, interpolating LiDAR points into raster images causes significant loss of information. Therefore, instead of converting LiDAR point into raster images, all raw LiDAR points were explicitly classified into either ground points or non-ground points. The terrain surface which is created at the end of the iteration is used as the basis for point classification. If the orthogonal distance is less than 0.3 m, those points are classified as ground points and others are assigned as non-ground points. Offset distance threshold was selected by doubling typical vertical accuracy of the ALTM 1233 laser mapping system (15 cm). These classified points were compared to the reference plot data sets and used for final accuracy assessment.

2.2.2 Test site and data

2.2.2.1 Test site

To evaluate this method, we performed our analysis at the Angelo reserve area (39° 45' N; 123° 38' W; 430-1290 m elevation), which is a component of the University of California Natural Reserve System (NRS) in Mendocino County, CA. This site is particularly adequate for our purpose (evaluating the performance of a non-terrain filtering method) because this area consists of heterogeneous mixed forests with various density and a steep topographic slope. In other words, the site well represents difficult conditions for separating ground and non-ground points from raw LiDAR data in automated procedures. In north-facing slopes, old conifer species are dominant (*Pseudotsuga*) mixed with broadleaf trees (*Lithocarpus*). On other aspects, tanoak is less frequent than *Quercus* species (*Pseudotsuga*-mixed hardwood forest) compared to the north-facing slope (Hunter and Barbour, 2001; Polis et al., 2004). We used a study site of size 4 km^2, which is a subset of the entire data set (180 km^2) of the South Fork Eel river watershed.

2.2.2.2 LiDAR data

LiDAR data used in this study were generated by the NSF-supported National Center for Airborne Laser Mapping (NCALM). Airborne laser scanning was performed on June, 2004. The data were acquired by the ALTM 1233 laser mapping system (Optech Inc) mounted on a fixed wing airplane. The laser pulse frequency is 33 kHz and the swath width is 20 degrees per half angle. The datasets include the first and last pulses for x, y, z coordinates, intensity value, and GPS time. Combined with inertial navigation and kinematic GPS, this system provides absolute elevation of the ground surface with vertical accuracy of 15 cm in open areas. The density of LiDAR points is varied by flight height, ground surface elevation changes, and overlap between swaths. The average point density of this study is 3.1 pulses per square meter (first and last returns combined).

2.2.2.3 Reference plots

Because the main object of this study is to separate ground and non-ground point from raw LiDAR point clouds, the performance is accessed by accuracy of filtering non-ground points rather than absolute elevation errors. Several research studies conducted field measurement of reference points with a combination of total station and GPS units (Hodgson and Bresnahan, 2004; Kobler et al., 2007; Reutebuch et al., 2003; Bater and Coops, 2009)

Sithole and Vosselman (2004) created the reference data for their comparison of filter algorithms by the manual point interpretation method. In addition, Kobler et al. (2007) suggested that manual filtering is the best possible method given no additional information. Accordingly, we manually created the reference data from the original LiDAR point cloud. Because point density is high enough to depict ground surface and non-ground object (e.g. tall trees and sub-canopy vegetation), we were able to create reference data by manual interpretation of three dimensional LiDAR point plots. Non-ground points were carefully selected and removed by 3D

visualization software (Quick Terrain Modeler, Applied Imagery). Only terrain points remained and assigned as terrain points and all the other points are assigned as ground points. By this visual interpretation procedure all points were explicitly assigned either “ground points” or “non-ground points” and used for selecting optimal parameters and assessing performance of this method. Even though we are familiar with this area, it is impossible to discover the pattern of LiDAR point distribution over the entire area before analyzing data sets. Thus, we placed 16 reference plots (10 m by 10m) systematically under the assumption that we did not have any prior knowledge of this site. The distance between plots is set to 200 m in two perpendicular directions (either North-South or East-West) so that plots were well distributed over the study site. Figure 2-4 shows the distribution of 16 reference plots.

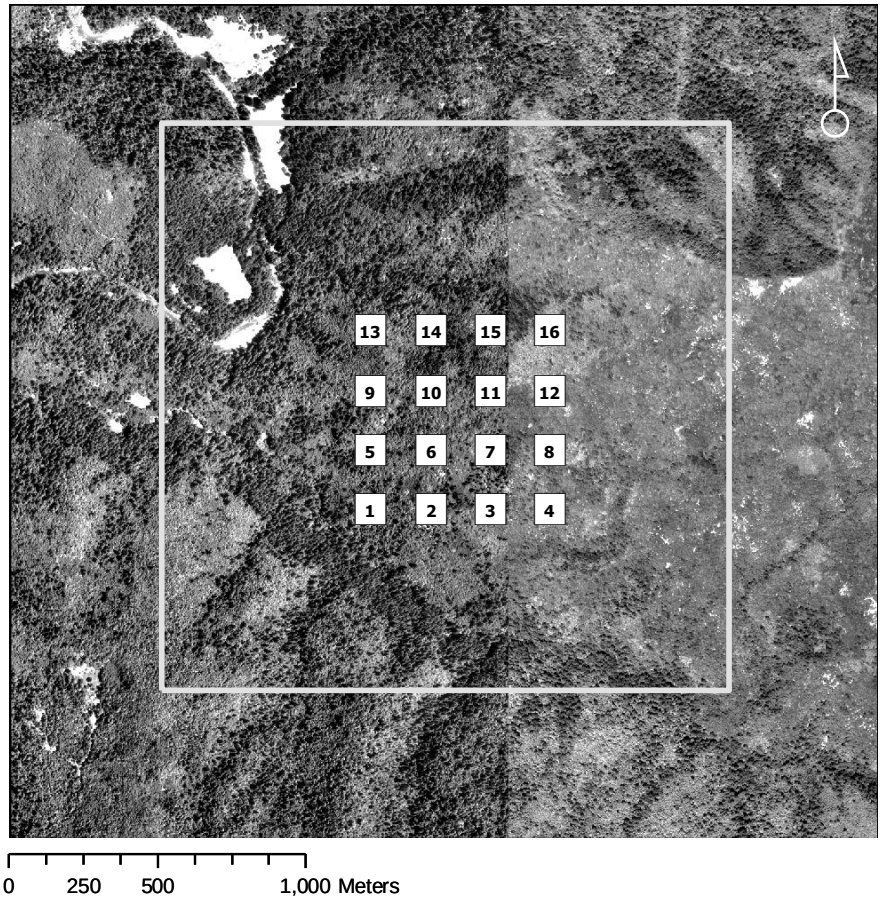

Figure 2-4. Reference plots (10 m by 10 m) in test area (4 km^2)

2.2.3 DEM for qualitative analysis

Even though the main purpose of this study is classifying raw LiDAR points into ground and non-ground points, we generated a DEM for visual inspection of classification quality. Because with a continuous surface is easier for the human eye to detect abnormal shapes, an interpolated surface is utilized to identify inaccurate LiDAR point filtering results. Evans and Hudak (2007)

suggested that thin-plate interpolation provides a better result than others, such as ordinary kriging and inverse distance weight. Accordingly, we used thin plate interpolation (TPI) for interpolating terrain point and creating DEM for visualizing terrain surfaces.

2.2.4 Parameter optimization

Optimal threshold (admissible angle) value is selected by comparing percent errors between different threshold values. For a quantitative analysis of this method, the filtering errors, which were produced by comparing the filtering result with the reference data, were investigated. There are two types of errors in filtering LiDAR data - Type I (omission) error and Type II error (commission). A type I error is to miss ground points even though the points are truly ground points and a type II error is to falsely classify non-ground points as ground points. Total errors can represent combined error (Type I and Type II). However, it is considered that the total number of errors are greatly influenced by the proportion between ground and non-ground points (Sithole and Vosselman, 2004).

2.3 Results

2.3.1 Parameter selection

The PTF method requires 3 parameters: 1) angle threshold between a triangular surface and a node point, 2) distance threshold, and 3) grid size for initial seed points. Because distance threshold is intended to remove only outliers (either positive or negative), it does not have a huge impact if there is no outlier in the raw LiDAR points. We used 100 m for both positive and negative direction. Also, the result is not sensitive to the grid size for the initial seed points. A grid size for initial seed points can be selected based on the largest non-ground object (e.g. building) within the filtering area (Axelsson, 2000). In this study, there is no large artificial object in the filtering area so that a value is set to 32 m, which is larger than the canopy diameter of tall trees. Angle threshold is the key parameter to decide performance of this method. It is important to determine an adequate threshold value to maximize filtering performance. In this study, we used 16 systematically distributed plots to assess the performance of this method.

As an admissible angle is enlarged, Type II errors (falsely accept non-ground points as ground points) are decreased but Type I errors (misclassifying true ground points as object points) are increased. If an admissible angle is decreased, Type II errors are increased and Type I errors are reduced. Depending on the priority in filtering purpose, the balance between Type I and Type II errors can be adjusted. For example, minimizing Type II errors intends to remove as many non-ground points so that a terrain model from ground points does not create false peaks and spikes. However, it compromises the detail of the terrain surface by removing true ground points. Because the two error types react in an opposite manner, a total error can be use to assess the performance of certain methods. Figure 2-5 shows total, type I, and type II errors by different admissible angles (from 15° to 20°). As the angle threshold is increased, a Type I error is decreased, but a Type II error is increased. The minimum total error is acquired at the angle value of 18°. Table 2-1 shows the confusion matrix with angle threshold 18° (all 16 plots

combined). 10.71 % of ground points (48 out of 448) were misclassified as non-ground points (Type I error) and 0.72 % of non-ground points (35 out of 4,893) were falsely classified as ground points (Type II error). The total error is 1.55 % and the total error is mostly influenced by Type II error because non-ground points have a large proportion of all plots.

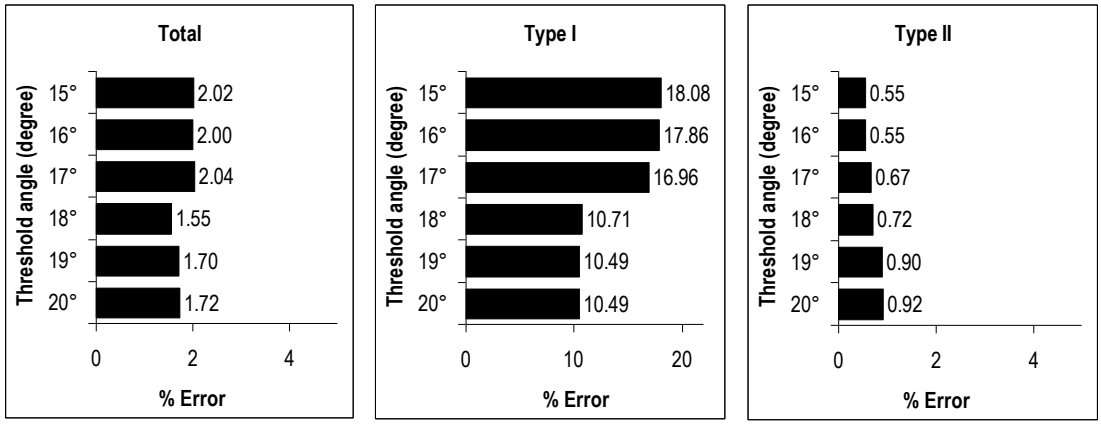

Figure 2-5. The result of total, type I, and type II errors by different admissible angles

Table 2-1. Accuracy assessment table (angle threshold: 18°). BE (Bear Earth), OBJ (Object)

		Filtered		*Total points*	*Error*	
		BE	*OBJ*		*Type*	*%*
Ref.	*BE*	400	48	448	I	10.71%
	OBJ	35	4858	4893	II	0.72%
	Total	435	4906	5341	Total	1.55%

2.3.2 Error analysis by plot characteristics

Even though the plots were selected by a systematic sampling scheme, certain plots are able to represent different filtering conditions so that we can recognize the source of errors and optimize the threshold value for the best performance in this type of heterogeneous forested area with steep hill slope. Table 2-2 shows total, type I and type II error for the 16 reference plots.

A Type I error at Plot 9 is 95.3% with 15° angle threshold and the error is changed to 25.6% with a 20° angle threshold. Because plot 9 is located on a steep ridge line, a small angle threshold is not able to detect ground points during iteration procedures so that this plot shows a large type I error at the low angle threshold. We found that a value of 18° is the minimum threshold to retrieve correct terrain shapes for this plot. Plot 1 and plot 10 show similar results (with less magnitude) because both plots are also on ridge lines. For plot 4 and plot 12, Type II

errors are increased as angle threshold is increased. These plots have relatively low vegetation so that it is more likely to falsely detect non-terrain point (low vegetation) as terrain points. Other plots (2, 3, 5 to 8, 11, 13 to 16), are not sensitive to angle threshold and show almost the same amount of errors regardless of error types. This is because these plots have large gaps between terrain surfaces and canopy layers (tall trees) so that the confusion between ground and non-ground points is less likely to happen.

Table 2-2. Confusion matrix by reference plots. Total, Type I, and Type II errors

Plot #	Total error (%)						Type I error (%)						Type II error (%)					
	Angle threshold (°)						Angle threshold (°)						Angle threshold (°)					
	15°	16°	17°	18°	19°	20°	15°	16°	17°	18°	19°	20°	15°	16°	17°	18°	19°	20°
1	0.6	0.6	0.6	0.3	0.3	0.3	0	0	0	0	0	0	28.6	28.6	28.6	14.3	14.3	14.3
2	1.8	1.8	1.8	1.8	1.8	1.8	0	0	0	0	0	0	26.3	26.3	26.3	26.3	26.3	26.3
3	0.4	0.4	0.4	0.4	0.4	0.4	0	0	0	0	0	0	4.8	4.8	4.8	4.8	4.8	4.8
4	2.1	2.1	2.1	2.1	5.3	5.3	2.3	2.3	2.3	2.3	5.7	5.7	0	0	0	0	0	0
5	0.0	0.0	0.0	0.0	0.0	0.0	0	0	0	0	0	0	0	0	0	0	0	0
6	0.3	0.3	0.3	0.3	0.3	0.3	0	0	0	0	0	0	6.3	6.3	6.3	6.3	6.3	6.3
7	1.4	1.4	1.4	1.4	1.4	1.4	0.6	0.6	0.6	0.6	0.6	0.6	8.1	8.1	8.1	8.1	8.1	8.1
8	1.3	1.3	1.3	1.3	1.3	1.3	0	0	0	0	0	0	11.1	11.1	11.1	11.1	11.1	11.1
9	10.1	10.1	9.4	3.2	3.2	3.2	0	0	0	0.6	0.6	0.6	95.3	95.3	88.4	25.6	25.6	25.6
10	2.9	2.6	3.4	3.4	3.1	3.1	0	0	1.2	1.2	1.2	1.2	29.7	27.0	24.3	24.3	21.6	21.6
11	0.3	0.3	0.3	0.3	0.3	0.3	0	0	0	0	0	0	1.4	1.4	1.4	1.4	1.4	1.4
12	7.3	7.3	8.0	8.0	8.0	8.0	6.3	6.3	7.0	7.0	7.0	7.0	30.8	30.8	30.8	30.8	30.8	30.8
13	0.3	0.3	0.3	0.3	0.3	0.3	0	0	0	0	0	0	14.3	14.3	14.3	14.3	14.3	14.3
14	0.7	0.7	0.7	0.7	0.7	0.7	0	0	0	0	0	0	5.8	5.8	5.8	5.8	5.8	5.8
15	0.3	0.3	0.3	0.3	0.3	0.6	0	0	0	0	0	0.3	7.1	7.1	7.1	7.1	7.1	7.1
16	0.3	0.3	0.3	0.3	0.3	0.3	0	0	0	0	0	0	3.6	3.6	3.6	3.6	3.6	3.6

2.3.3 Qualitative assessment of filtering performance

Although we performed quantitative analysis by a contingency matrix with 16 reference plots data, we also performed qualitative analysis by visual inspection of the interpolated DEM. Figure 2-6 shows DEM created from ground points for qualitative analysis. The angle threshold value is set to 18°, which is acquired from previous procedures. This angle threshold is large enough to remove all major Type I errors (omission errors) in the area so that we cannot detect major loss of terrain surface description. However, it falsely classifies low vegetation points as ground points and we can detect commission errors at south facing slopes, which are covered by low vegetation.

2.4 Discussion

The result from our study shows one universal threshold value cannot perform optimally for all types of terrain characteristics. Even though a threshold value can be adjusted by a user's preferences, more study should be conducted to optimize a threshold value with minimum user interventions. The major limitation of our method is to use one universal threshold value for the entire level of filtering procedures. We found different threshold values are required for different levels of scale (especially coarse-to-fine scale approaches). For example, relatively large threshold values are needed only for the early stage of terrain approximation so as not to omit terrain points, and smaller threshold values are preferred to reduce commission errors (falsely detect low object points as terrain points).

Although this method has been developed for complex forested areas with steep terrain slopes, we need to test the performance of this method for different environmental conditions.

Also, for more objective comparison with other filtering method, we need to perform our method with common data set and reference data, such as The ISPRS Commission III/WG3 dataset (Sithole and Vosselman, 2004).

2.5 Conclusion

In this study, the Progressive Terrain Fragmentation (PTF) method is developed to improve the performance of filtering non-terrain points from raw airborne laser scanning data. Iterative procedures for searching terrain points gradually approximates terrain surface. Instead of using absolute slope or offset distance, this method utilizes orthogonal distance to and relative angle between a triangular plane and a node. For that reason, PTF was able to classify raw LiDAR points into ground and non-ground points on a heterogeneous steep forested area with a small number of parameters. We found "admissible angle" is the most influential parameter for accurate filtering procedures. We found a smaller admissible angle threshold causes inaccurate terrain approximation by omitting terrain points around ridge lines. On the contrary, a large admissible angle threshold brings failure to remove low vegetation. The optimum threshold value for admissible angle was selected by examining 16 reference plots, which minimizes the total number of errors for classifying raw LiDAR points. Classifying raw LiDAR points (ground vs. non-ground) for generating terrain surface is a basis for other analysis related to forest biophysical parameter extraction. Thus, we expect our study will provide more accurate terrain approximation and contribute to improving extraction of other forest biophysical parameters.

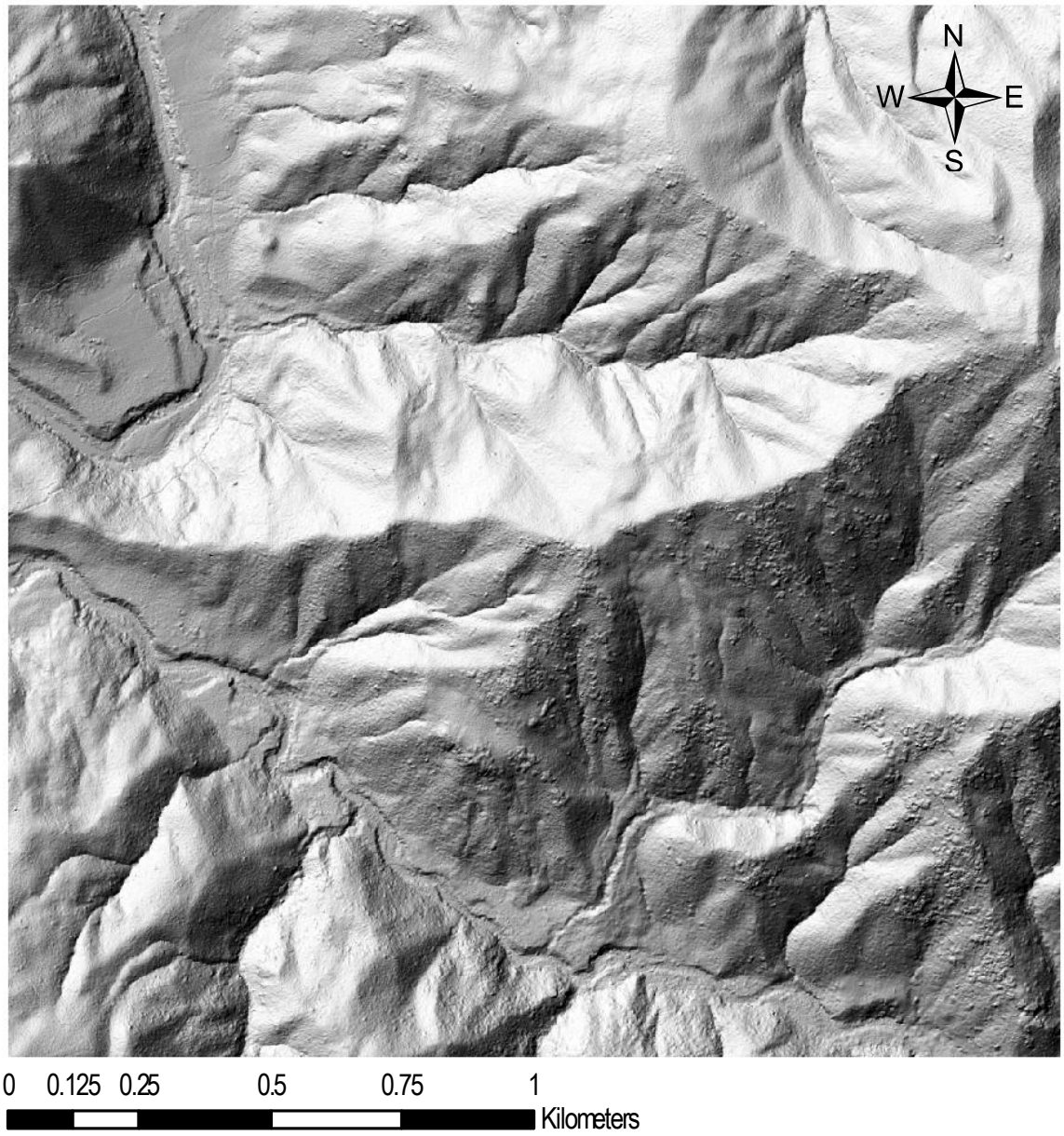

Figure 2-6. Shaded relief map of DEM by 18° angle threshold. (1 m grid cell size, thin-plate interpolation)

Chapter 3 Detecting and delineating individual trees in a heterogeneous forest using airborne LiDAR data

3.1 Introduction

Forests, as major components of the land surface, have important roles to sustain the Earth's ecosystems. However, forested areas have rapidly decreased because of the demand for resources and land use by population growth (Franklin, 2001). In addition, these decreasing forest areas and increasing fossil fuel consumption have been altering global climate ((Houghton et al., 2001). Forest disturbances are increasingly caused by climate change and these disturbances threaten the sustainability of forest ecosystems (Millar et al., 2007; Dale et al., 2001). Thus, continuous and precise monitoring and assessments of large forest areas are critically required. Although precise measurements of individual trees can be gathered by field measurements, field measurements are labor intensive and time consuming especially for enough measurements over large and heterogeneous forest areas. Therefore, we need automated and accurate methods which can supplement field measurements. High spatial resolution remotely sensed data can be applied for this objective because developing technologies keep increasing spatial resolution and make it possible to handle large amounts of remotely sensed digital data by powerful computers at reasonable prices.

Among the various remote sensing methods, discrete-returns, small-footprint LiDAR systems are highly effective for extracting detailed forest biophysical parameters, because LiDAR can provide detailed 3-dimentional surfaces (both canopy and ground) data with high spatial resolution and accuracy (Lim et al., 2003; Reutebuch et al., 2005). There have been extensive attempts to extract forest biophysical parameters from LiDAR data. Hyyppä et al. (2008) categorized those methods into two approaches which are based on statistical canopy height distribution and individual tree detection. Previously, distribution based methods were more commonly used because these methods can be used even when the point density is not high enough to isolate an individual tree (Holmgren, 2004; Naesset, 2002).

As the sensing technology has developed, individual tree based methods are gaining utility. Compared to distribution-based methods, individual tree based methods require less amount of field measured reference data for calibration to extract forest physical parameters. In addition, individual tree based methods provide more precise information especially in heterogeneous forest structures (Hyyppä et al., 2008; Koch et al., 2006). A variety of methods for identifying and delineating individual trees have been elaborated. Koch et al. (2006), Leckie et al.(2003) and Maltamo et al.(2004) extracted local maxima from the canopy surface model (CSM) to detect individual trees from LiDAR data and delineate canopy boundary by segmentation methods. Popescu et al. (2003) improved individual tree detection by applying variable window sizes (filtering) selected by the relationship between the height of the trees and their crown size. Andersen et al (2001) and Chen et al. (2006) used morphological image processing techniques to isolate a single tree from canopy height model (CHM) generated from LiDAR data. As for individual tree delineations, it is common to use a raster surface model interpolated from raw LiDAR points (Wang et al., 2007). However, because the process of interpolating from discrete LiDAR points to a raster model always causes loss of information, there have been several attempts to use raw LiDAR points rather than interpolated a raster surface model (Morsdorf et al., 2003; Wang et al., 2007).

The correct detection and delineation of an individual tree from LiDAR data is an important prerequisite for achieving precise forest biophysical parameters (such as tree counts, crown volume, canopy closure, tree height, diameter at breast height distribution, volume, and biomass) because all the subsequent estimation could contain propagated errors from the initial individual tree isolation (Koch and Dees, 2008; Koch et al., 2006).

The objective of this study was to develop a method to detect tree tops and delineate an individual tree crown with a LiDAR driven digital surface model as well as with raw LiDAR point clouds. Prior to tree top detection and delineation, we divided our study site into two height classes (high and low trees). For high trees, we applied the marker-controlled watershed segmentation for delineating a single tree from the digital surface model (similar to Chen et al. (2006)'s approach). However, we detected tree tops (markers) directly from raw LiDAR points instead of interpolated surfaces by using a progressive filter size (from large to small), so that our approach does not require steps to optimize the parameters to detect tree tops. In addition, we conducted an additional verification procedure to reduce false tree top detection by using the shape of canopy profiles between trees. For low trees, instead of a progressive filtering size, we used a small fixed window-size local maximum filter (1 m radius) to detect tree tops and applied the skeleton by influence zones (SKIZ) segmentation to delineate crown boundaries. We refined the crown boundaries by removing the crown areas, which were lower than the mean elevation of each canopy boundary.

3.2 Study Sites and Materials

3.2.1 Study Site

The study site of this research is located at the Angelo Coast Range Reserve, part of the University of California Natural Reserve System on the South Fork of Eel River in Mendocino County, CA. The Angelo Coast Range Reserve is mainly covered by mixed evergreen forests (Hunter and Barbour, 2001). This site is dominated by *Pseudotsuga menziesii* (Douglas Fir), *Sequoia sempervirens* (Coast redwood), and mixed deciduous trees, such as *Lithocarpus densiflorus* (tanbark oak), *Arbutus menziesii* (madrone), and *Quercus kelloggii* (black oak) (Kotanen, 2004; Power et al., 2004). The elevation ranges from 378 – 1290 m. Average temperatures range from 16 – 31℃ (UC Natural Reserve System, 2010). We used a subset (0.15 km^2) of the larger 180 km^2 of the South Fork Eel river watershed to develop and evaluate our method to delineate individual tree crowns (Figure 3-1)

3.2.2 Data

Both the LiDAR data and aerial photography were acquired simultaneously on the same airplane on June 29th, 2004. In this study, LiDAR data were mainly used for the analysis and aerial photographs were used only for visual reference purposes. LiDAR data were recorded by Airborne Laser Swath Mapping (ALSM). The ALSM system is composed of an Optech Inc. model 1233 Airborne Laser Terrain Mapper (ALTM) unit, Differential Global Positioning System (DGPS) and Inertial Measurement Unit (IMU). The laser pulse frequency is 33 kHz and swath width is ±20º. The datasets have the first and last returns for x, y, z coordinates, relative intensity value (from a 1064-nm laser), and GPS time. The system obtains 2-3 pulses per 1 m^2 with vertical accuracy of 15 cm. Simultaneous to LiDAR data, digital aerial photographs were acquired by an optical 3-Charge-Coupled Device (CCD) digital multispectral camera (Redlake

MASD Inc., model MS4100). The resolution is 1920(H) x 1080(V) with 3 visible bands (R,G,B). The images have roughly 15-20 cm spatial resolution at 600-800 m flight height.

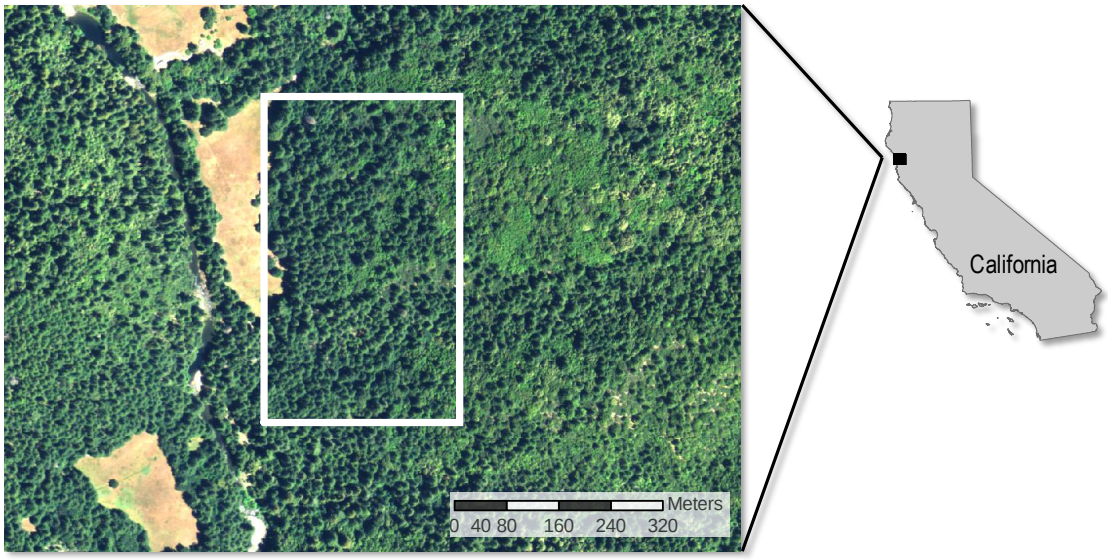

Figure 3-1. Overview of the study site. The background image was created from the National Agricultural Imagery Program (NAIP).

3.3 Methods

The proposed method for detecting and delineating individual trees from airborne LiDAR data is composed of four main steps; (a) data preparation, (b) tree top detection, (c) crown delineation, and (d) crown boundary refinement. The procedures of our method are presented in Figure 3-2.

3.3.1 Preprocessing

Although LiDAR data contain information for canopy and terrain surfaces, it is necessary to separate and extract both surfaces from the original raw LiDAR points. To extract trees from LiDAR data, it is common to calculate canopy height (Canopy Height Model; CHM) by subtracting a ground elevation model (Digital Terrain Model; DTM) from a canopy surface model (Digital Surface Model; DSM) . In our study, we used the Progressive Terrain Fragmentation (PTF) Algorithm to extract the DTM from the raw LiDAR data (Lee, Chapter 2). The PFT method is suitable for our site which has heterogeneous tall conifer trees with steep hill slopes. The PFT method prioritizes a set of LiDAR points, which are used to approximate a triangulated irregular network (TIN) surface, so that important terrain points are added earlier than the other points, and we can minimize the possibility of including false-ground points during the iteration process.

For tree top detection, we used discrete pixels of raw LiDAR points instead of an interpolated continuous surface model (i.e. CHM), because we intended to minimize the influence of interpolation errors. Although we used discrete point data, the raw LiDAR points were converted to discrete raster pixels for efficient neighborhood operations (Wack et al., 2003). When multiple points existed within in one pixel, the highest point was selected and the height of the point was assigned to the pixel value. Consequently, this conversion procedure reduced the

amount of data points and improved the efficiency of calculations (data thinning effect). A spatial resolution of the raster data was set to 0.25 meters, which was an approximate footprint diameter of LiDAR pulses (average flight height of 800 m). The aboveground height of each pixel was calculated by subtracting the ground elevation value of the DTM from the surface elevation value of each pixel.

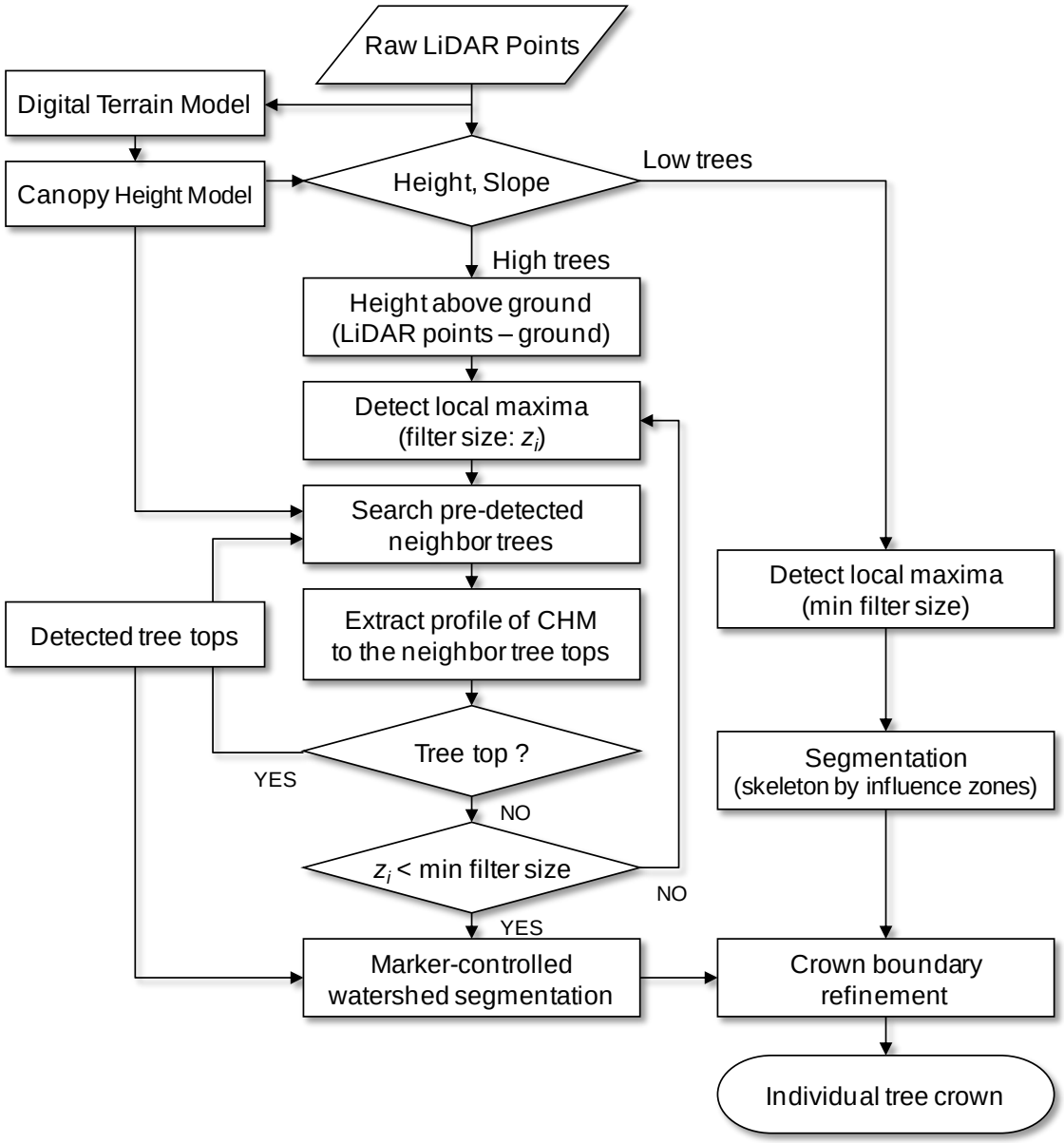

Figure 3-2. Flow chart of the procedures used in the study

Even though we used discrete pixels of raw LiDAR points for tree top detection, the CHM was prepared to delineate crown boundaries and extract canopy profile information between tree tops. Because the CHM was calculated by subtracting the DTM from the DSM, the DSM should be created before the CHM. The DSM was generated with the highest elevation

point from either first or last returns for each cell location. In theory, last returns should be reflected from the ground under the canopy in forested area. However, when there is only one return which is strong enough to be recorded, it is recorded as a last return. Therefore, some points recorded as last returns might be actually from the outermost surface. Thus, we used both first and last returns to generate the DSM. As the laser beam has an ability of passing the canopy of trees, we can extract both a tree canopy surface and a ground surface from LiDAR data. However, this ability causes large height variance especially in structurally heterogeneous conifer forests. Because a large portion of our study sites is also dominated by tall conifer trees, the ability of canopy penetration causes small holes and pitfalls in canopy surface reconstruction. These small holes are problematic when the crown boundaries of individual trees are determined by the shape of the canopy surface. In order to remove these errors, these small holes were detected by a morphological operation (extended-minima transform). We applied the extended-minima transform to detect the points which caused small holes and pitfalls and excluded those points when we constructed the DSM. The extended-minima transform is the regional minima of the h-minima transform (Soille, 2003). Thus, the extended-minima detected all regional minima (holes) in the image whose depths were deeper than a certain threshold (*h*). We selected 5 meters as the h value, which is large enough to remove only falsely created holes. "Then, the points, which caused these minima, were excluded for reconstructing CHM. Figure 3-3 shows the effect of removing small holes in the CHM.

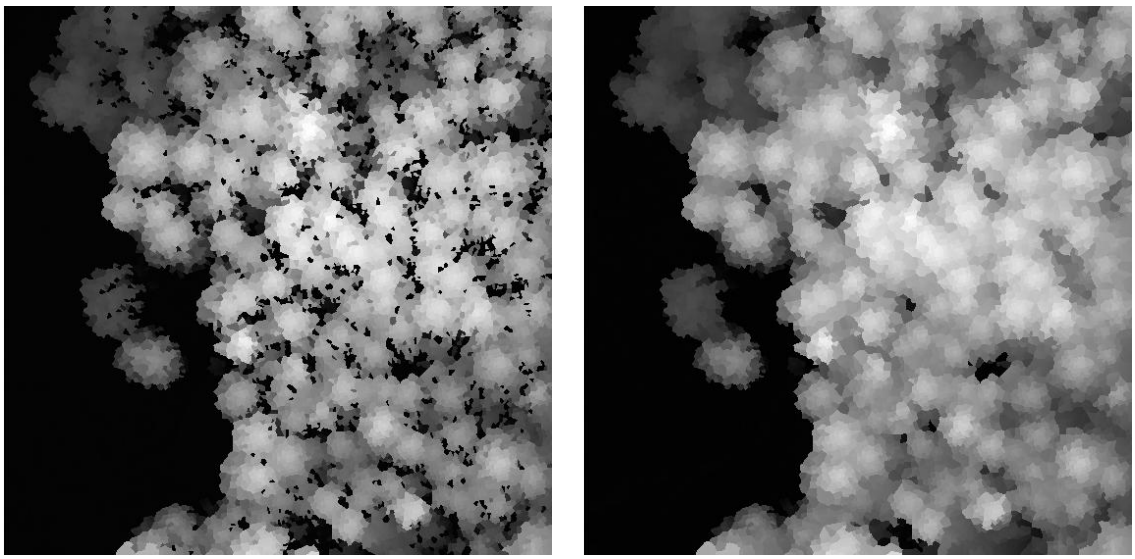

(a) (b)

Figure 3-3. Effect of removing small holes and pitfalls from CHM by using the extended-minima transformation. (a) CHM before removing small holes. (b) CHM after small holes were detected and removed.

Because the study site was composed of two distinct canopy structures (very tall conifer trees and small deciduous trees), we separated the region into two classes based on the height of the canopy and canopy shapes (the slope of canopy surface). When the height of the canopy was smaller than 25 m and the slope of canopy surface was lower than 45°, the region was classified as low trees. Otherwise, the region was classified as high trees. For high trees, a progressive filter

size was applied to detect tree tops, followed by marker controlled watershed segmentation to delineate crown boundaries. For low trees, tree tops were detected using a small fixed window-size local maximum filter (1 m radius) and the crown boundaries were segmented by using the skeleton by influence zones.

3.3.2 Tree Top Detection

In general, an individual tree crown has a convex shape, so that the tree tops can be detected by selecting the peak (local maxima) of the canopy (Popescu et al., 2003). It is critical to select an appropriate window size for detecting trees from images. However, it is not simple because trees have different shapes and sizes. If the window size is too large, there would be a lot of omission errors (missing trees tops). Conversely, if the window size is too small, large number of local maxima would be incorrectly detected as tree tops. So, it is difficult to find an optimal window size to perform the best for all different site conditions. The relationship between tree height and crown width was adopted to decide appropriate window sizes (variable window-size) to detect tree tops from LiDAR data (Popescu and Wynne, 2004; Chen et al., 2006; Wack et al., 2003). Although the variable window-size method performs better than the fixed window-size method, the variable window-size method still requires priori knowledge about the relationship between tree height and canopy width. Because the parameters to describe this relationship are site and species specific, different site conditions need different parameters. In addition, if the relationship between tree height and canopy width is not strong enough, and the variance of canopy width is large (asymmetrical shape), the improvement of accuracy by using variable window-size method would be limited.

In this study, we used the discrete canopy height pixels, which represent raw LiDAR points in raster data model, in order to minimize the errors during the surface interpolation and smoothing procedures (Wack et al., 2003). We applied a progressive window-size (from large to small) filter to detect local maxima. Then, the geometric characteristics of a canopy profile were used to justify if the detected point is a true tree top.

First, local maxima points were searched by a relatively large window size to detect tree tops. Then, the window size was progressively decreased to detect omitted tree tops at the previous level. For each detected tree top candidate, additional procedures were applied to evaluate whether the detected local maximum point was a true tree top or not. When the candidate point was classified as a tree top point, the point was added to a set of detected tree top points and used as pre-existing tree tops for the following neighbor searching step. In contrast, if the tree top was classified as a false tree top, the point was marked as a non-treetop point and excluded for the following tree searching procedures. Under the assumption that trees have convex shapes and tree tops have relatively higher elevation compared to their connected neighbor canopies, a valley should exist between two tree tops. We used the CHM profile between two local maxima points (candidate point vs. neighbor treetop point) to extract and assess geometric characteristics. If a local minimum (valley) can be detected in the profile of the CHM, we can classify the candidate point as a true tree top. If the tree top is not present in the CHM, there is no local minimum in the profile of the CHM. Thus, the tree top cannot be detected correctly. In this case, the gradient of the CHM profile can be used to depict a weak tree top as a peak (see **Figure 3-5**(b)). The magnitude of the gradient increases from the tree top to the valley, decreases toward the other tree top, and increases again passing the other tree top (the gradient is always calculated in the direction from the higher tree top to the lower tree top).

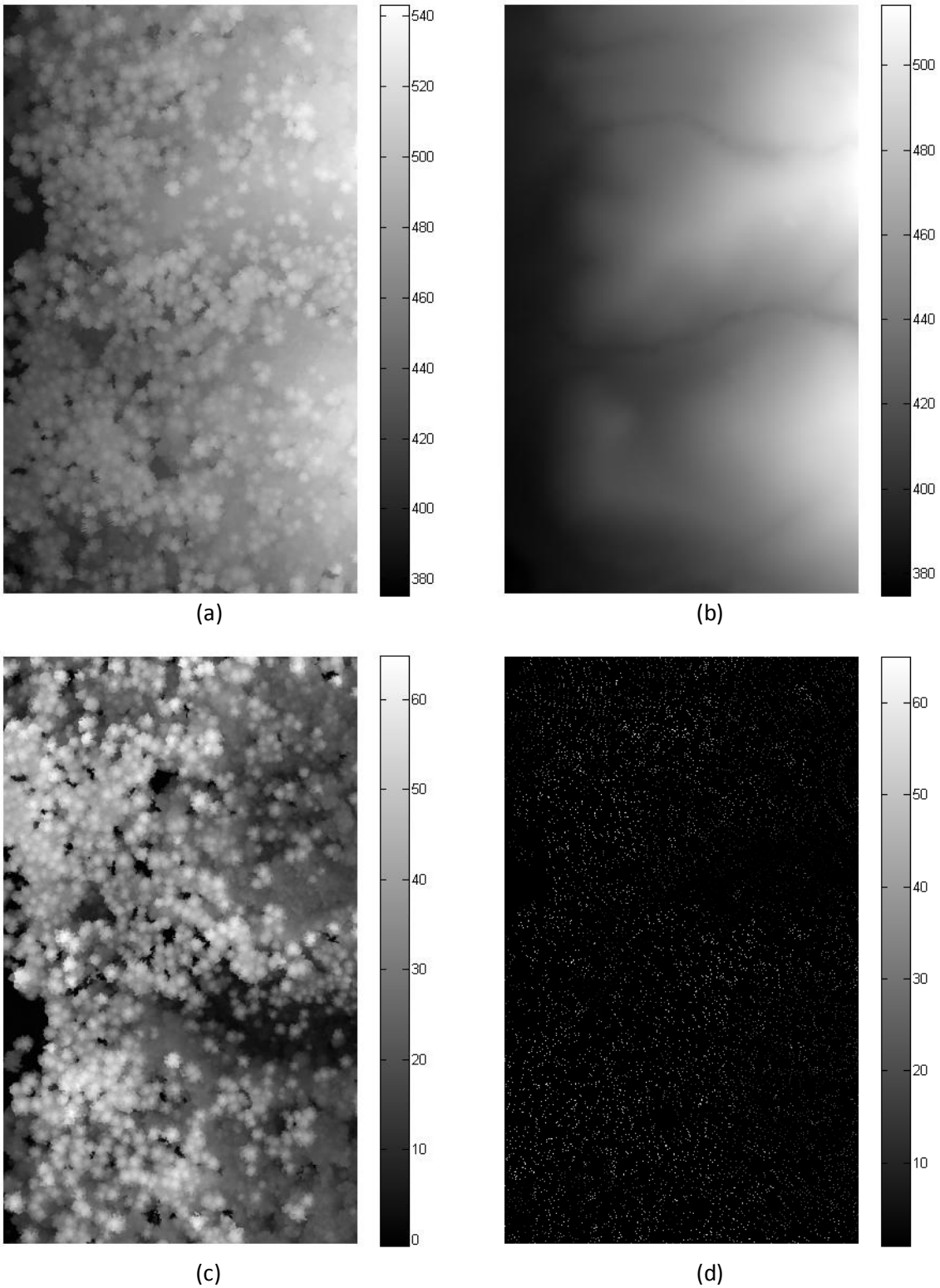

Figure 3-4. The data sets prepared to detect and delineate individual trees from the LiDAR data. (a) DSM, (b) DEM, (c) CHM, and (d) LiDAR pulses for a progressive local maximum filter to detect tree tops

If the peak (local maximum) exists on the gradient of CHM and the peak value is greater than a certain value, the condition is satisfied (the peak is considered as distinctive tree top). The threshold value for the gradient in the profile was set to -0.2 based on several attempts for our site. We found that this threshold value performed consistently for all sizes of trees if canopy shapes were not very different. When the conditions for all directions are accepted, the point is classified as a true tree top. The method steps are summarized:

- Create strongly smoothed CHM. Gaussian filtering with α = 15 pixels (3.75 m);
- Search local maxima value with progressive filter size (large to small);
- Sort detected tree top candidate points in descending order;
- Search pre-existing neighbor tree tops of the candidate point by Delaunay triangulation;
- Reconstruct the profile of CHM and the gradient of the CHM from the higher point to the lower point direction;
- Access the geometric characteristics of the profile. The pseudo code of the procedure is:

```
If local minima exist?
        The candidate point = true tree top
Else
        If gradient value of local maxima > - 0.2
                The candidate point = true tree top
        Else
                The candidate point = non-treetop
        end
end
```

- Repeat above procedures until the filter size reaches the minimum size (1 m radius).

Our method applied progressive window-size (large to small) filters to detect local maxima point from 3D points. Then, the detected local maxima points were verified if the point was a true tree top or not based on the profile of the CHM and the gradient of CHM among the candidate point and the neighbor tree tops. Because local maxima were searched by a progressive window-size filter, our method detected tree tops over the all scales. In addition, using the gradient of the CHM for assessing geometric characteristics reduced omission errors by strongly smoothed surface model and prevented commission errors by small filter sizes. **Figure 3-5** shows the example of tree top verification procedures. The detected potential tree top is represented as "P" and the neighboring trees are represented "T_1 to T_6" in **Figure 3-5**(a). The profile of the CHM (T_3 to P direction) is plotted in solid line in **Figure 3-5** (b). It has a local minimum value (valley shape) between the candidate peak and the neighboring tree top so that we can verify that two tree tops are distinctive for this direction. **Figure 3-5**(c) shows that the profile of CHM does not have a local minimum value between two points (T_1 and P) so that the profile of the CHM cannot verify the potential tree top and the neighboring tree are distinctive. In this case, the gradient of the CHM profile (dashed line in **Figure 3-5**(c)) is additionally used to check if the candidate point is a true tree top or not. Because the peak (local maximum) exists in the gradient of the CHM profile between the candidate point and the neighboring tree top, we can verify two tree tops are distinctive for this direction.

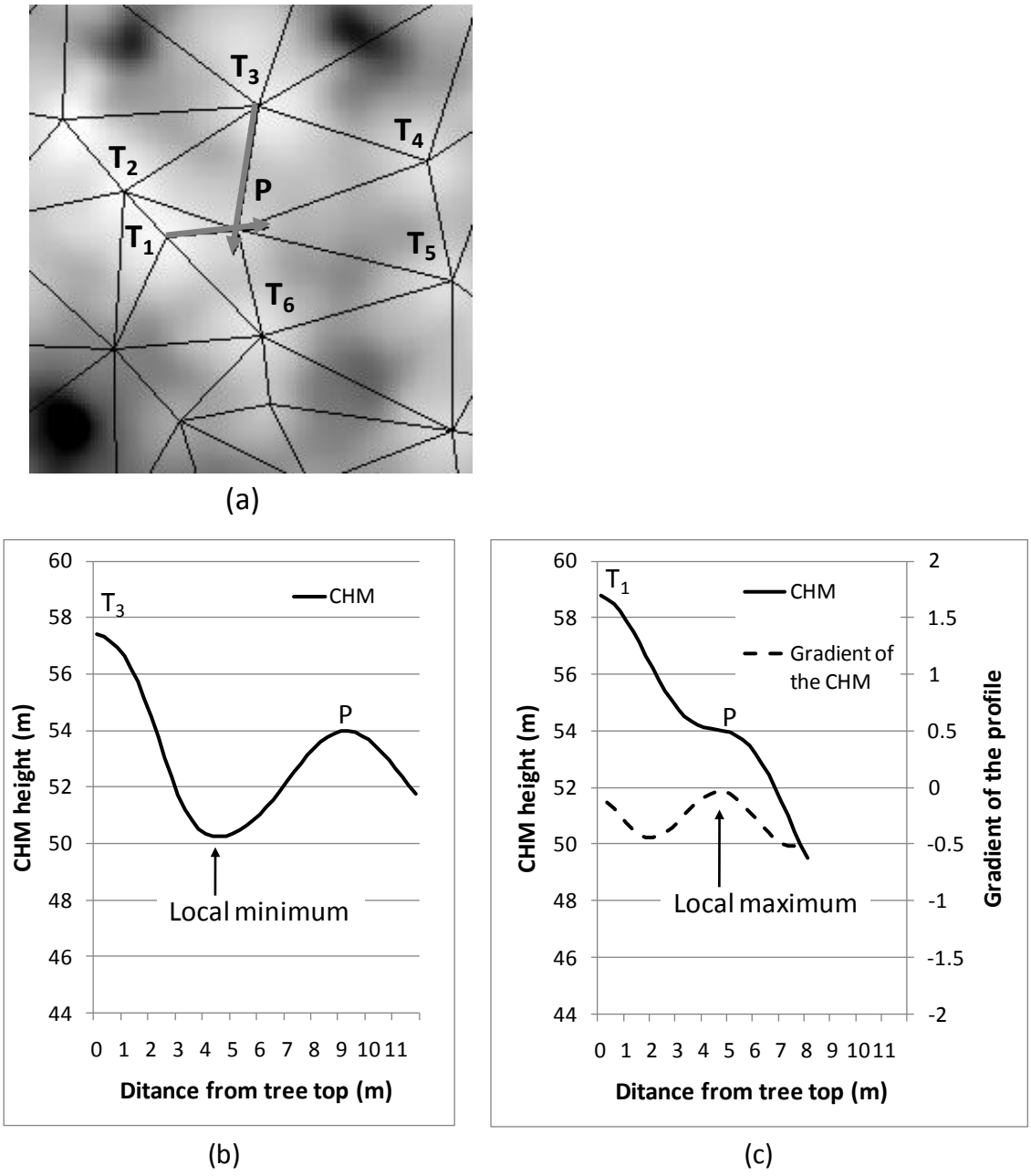

Figure 3-5. Example of the verification of detected tree tops. (a) Representation of CHM and tree tops. P is a candidate tree point and T_1 to T_6 are previously detected neighboring trees. The profiles between the candidate tree top (P) and each neighbor tree (T_1 - T_6) are tested. (b) The profile of DCM (T_3 to P direction). (c) The profile of DCM (T_1 to P direction) and the gradient of the profile

For low trees, a small fixed filter size (1 m radius) was used to detect tree tops. Because the LiDAR point density of our data was not high enough to depict the characteristics of the canopy surface, the progressive window-size local maximum filter did not performed effectively in detecting and separating individual trees. Thus, we employed a small fixed window size to

search the local maximum point as a tree top and omitted additional verification steps, which applied for high trees.

3.3.3 Crown Delineation

Watershed segmentation is an effective method to delineate boundaries of individual trees, because watershed segmentation is applicable to a wide range of scales and it performs well for the segmentation of height data (Straub and Heipke, 2007). Conceptually, the watershed segmentation is similar to a gradual immersion of a basin. Assume that each basin has a hole at its minimum elevation and water begins to flood areas adjacent to each hole. Adjacent basins are separated by "dams" so that divided basins are not merged in the segmentation process (Chen et al., 2006; Soille, 2003). Watershed segmentation commonly has over-segmentation problems because local minima points, which are used as seed points, are prone to being falsely detected. With marker-controlled segmentation it is possible to overcome this problem by correctly selecting markers, which are tree tops in individual tree delineation (Wang et al., 2004; Chen et al., 2006).

Although we used only point data for detecting tree tops, we used the CHM to delineate tree boundaries because, conceptually, the boundaries should be continuous and closed. In addition, creating a boundary can be performed more efficiently with continuous surfaces rather than with discrete points. Because the watershed segmentation is applicable to the basin shaped surface, the CHM was inverted so that local maxima became local minima and convex shaped canopy surfaces formed basins. Then, previously detected tree tops were used as markers for the segmentation.

In this study, we detected tree tops from LiDAR point data instead of the CHM. Thus, the seed points for the watershed segmentation were not local minima in the inverted CHM. In this case, the created boundaries might have incorrect shapes (thin and narrow shapes to the maximum slope direction). In order to prevent this problem, we used a small circular objects maker (1 m radius). For low trees, the marker-controlled segmentation with a small circular object marker frequently did not perform correctly. Although the radius of marker was small, when the distance among individual trees were smaller than the radius of the marker, multiple clustered trees were merged and incorrect boundaries were generated because the small markers overlapped each other. Instead of maker-controlled watershed segmentation, we employed the skeleton by influence zones (SKIZ) for low trees. The influence zone (IZ) is defined as the set of pixels of a binary image that are closer to a given connected component than any other connected component. The SKIZ is defined as the points that do not belong to any influence zone. The SKIZ operation produces the boundary of influence zone, which is equivalent to the Voronoi diagram (Soille, 2003; Whelan, 2001).

3.3.4 Crown Boundary Refinement

The watershed segmentation performs well when trees are close to each other. However, when the trees are adjacent to open spaces or have neighboring canopy gaps, the boundaries generated by the watershed segmentation are only poor approximations of individual crowns (Straub and Heipke, 2007). We employed two additional steps to correct these types of cases. First, when the trees were adjacent to open spaces, the crown boundaries could not be delineated correctly because the absence of markers for open spaces caused a failure of splitting tree crowns and open spaces. To cope with this problem, we created the boundaries between forested areas and open

spaces. Because the elevations of open spaces are near the ground elevation, we used 1.5 m as the threshold to separate open areas and forested areas. Then, we added this boundary when the marker-controlled watershed segmentation was conducted. Second, when large canopy gaps existed among trees, the gaps were included in the crown boundary of the neighboring trees. Hence, the segmented boundaries could not depict the actual crown edges. We assumed that incorrectly generated edges (outliers) have much lower elevation values compared to the average of all the crown edge elevation values. Accordingly, we calculated the average height of all the crown edge pixels and used this average value as the threshold value. The regions, which were lower than the threshold, were excluded from the canopy boundaries and the new boundaries were generated by this procedure.

3.3.5 Accuracy Assessment

To evaluate the accuracy of our crown delineation results, we prepared a reference crown map of our study site by manual delineation (Figure 3-6). We laid out 15 reference plots (30 m by 30 m) inside of our site in a systematic scheme. All the trees, located inside of the plot, were selected as reference trees. The crowns of the selected trees were carefully delineated from the CHM. Because the spatial resolution is very high (0.25 m), most of trees were visually identified with confidence in the laboratory. In addition, when the shape was not clear from the CHM, raw LiDAR points were visualized with 3D visualization software (e.g. ESRI's ArcGIS-ArcScene) and carefully examined from the various viewpoints and angles. Then, ortho-rectified aerial photos were separately used to verify the accuracy of crown delineation.

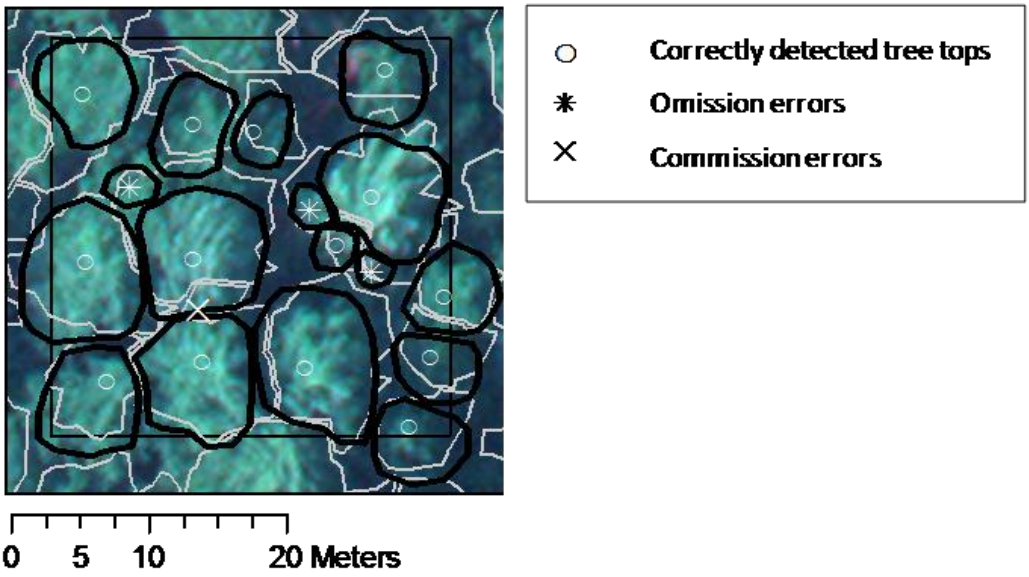

Figure 3-6. Example of accuracy assessment (from reference plot 2). Gray polygons indicate crown boundaries generated by our method. Black polygons represent reference crown boundaries created by manual delineation.

The comparison between automatically and manually extracted trees was conducted according to the overlapping area between a reference tree boundary and an automatically extracted tree boundary. If the ratio of the overlapping area (between the extracted boundary and

the reference polygon) to the reference tree crown area was greater than 0.5, we considered this as a correctly detected tree. We assumed only a one-to-one relationship between reference and extracted trees, and all the extracted trees counted only once. Hence, when there was more than one extracted tree crown overlapping with one reference tree polygon, the only one having the largest overlapping area was considered as a correctly detected tree. Conversely, when multiple reference tree polygons were contained by one extracted tree, only one tree was considered as the corresponding tree (if the overlapping area ratio was bigger than 0.5) and the others were considered as erroneously detected trees (commission errors). If a reference tree did not have a corresponding detected tree, the tree was classified as an undetected tree (omission errors).

3.4 Results and Discussion

Table 3-1 presents the accuracy assessment results. From the 15 reference plots in our study site, 442 trees were manually delineated to evaluate the performance of our method. The reference trees were split into two groups (high trees and low trees) as the criteria that we used previously. Among 442 trees, 180 trees were classified as high trees and 262 trees were classified as low trees. Overall, our method correctly detected 60.2% of trees. The percentage of missed trees was 39.8% and the percentage of falsely detected trees was 30.2%. For high trees, the proportion of correct, omitted, and committed trees were 71.1%, 28.9%, and 8.3%, respectively. For low trees, 52.7% of trees were correctly detected, whereas 47.3% of trees were missed and 19.8% of trees were erroneously detected. Figure 3-7 represents the final result of isolating individual trees by using LiDAR data in our site.

Because of inconsistency in accuracy assessment methods and differences in site conditions, it is difficult to compare our results with other studies directly. Persson et al. (2002) correctly detected 71% of all trees and 90% of larger trees (DBH > 20 cm). Maltamo et al. (2004) achieved 40% of accuracy for all trees and 80% of the dominant trees. Solberg (2006) got an accuracy of 93% for the dominant trees but 19% for the suppressed trees. Chen et al. (2006) isolated individual trees in deciduous forests with 64.1% of the absolute accuracy with much stricter accuracy assessment criteria than other methods. Although our method was applied in a structurally heterogeneous forest with steep slopes, we achieved 71.1% of accuracy for high trees and 52.7% of accuracy for low trees.

Table 3-1. Accuracy assessment of automatic tree isolation

	Reference		Correct		Omission		Commission	
	n	%	n	%	n	%	n	%
All	442	100.0	266	60.2	176	39.8	67	15.2
High trees	180	100.0	128	71.1	52	28.9	15	8.3
Low trees	262	100.0	138	52.7	124	47.3	52	19.8

Although the proposed method performed well for high trees, the errors were caused mainly by low trees. Because the crown shapes of low trees (deciduous trees) were less distinctive compared to those of high trees (tall conifer trees), it was more difficult to correctly detect tree tops. In addition, when the canopy size was too small, individual tree crowns did not have enough points (or pixels), so that the proposed method could not perform well enough to

isolate individual trees. In order to improve the accuracy of the tree detection and delineation, a higher pulse density is required so that the LiDAR data can depict crown shape more accurately.

Figure 3-7. The result of individual tree detection and delineation by the proposed method. White squares represent the reference plots used for accuracy assessment.

Comparison of different fixed-sized local maxima filtering methods

In order to compare our method to fixed window-size local maxima filtering methods, we applied different fixed window-size local maximum filters (4, 6, 8 and 10 m radius) to detect tree tops. Then, we delineated tree boundaries by the marker-controlled watershed segmentation. For the accuracy assessment, we employed the same criteria that we used for the assessment, which was used previously. The comparison between our method and fixed window-size local maximum filtering methods were summarized in Table 3-2. As expected, increasing the size of the filtering window increased the percentage of missed trees (omission errors). On the contrary, decreasing the size of filtering window increased the percentage of erroneously detected trees (commission errors). In order to represent all errors by one value and to compare different tree isolation methods, we calculated overall accuracy, which was proposed in Pouliot et al. (2002)'s research. The accuracy index (AI), which is defined as:

$$AI\ (\%) = [(n - (O + C)) / n] * 100$$

where n is the total number of the reference trees, O and C represent the number of omission and commission errors.

Table 3-2. Comparison of individual tree isolation accuracy by the proposed method and different fixed window-size local maximum filtering methods (4 m to 10 m radius)

	Our method	Fixed window-size local maximaum filters			
		r = 4m	r = 6m	r = 8m	r = 10m
ALL					
Omission	39.8%	52.0%	60.6%	65.2%	70.4%
Commission	15.2%	25.1%	9.3%	3.2%	0.7%
Accuracy Index	45.0%	22.9%	30.1%	31.7%	29.0%
High Trees					
Omission	28.9%	30.0%	38.9%	47.8%	56.7%
Commission	8.3%	58.3%	21.1%	6.1%	1.7%
Accuracy Index	62.8%	11.7%	40.0%	46.1%	41.7%
Low Trees					
Omission	47.3%	67.2%	75.6%	77.1%	79.8%
Commission	19.8%	2.3%	1.1%	1.1%	0.0%
Accuracy Index	32.8%	30.5%	23.3%	21.8%	20.2%

When the 4 m radius local maximum filter was applied, we acquired the lowest accuracy index (9.7%) because of the large percentage of commission errors (mostly from high trees). The commission errors were mainly caused by irrelevant surface fluctuations, which were falsely detected as tree tops. Increasing the window size of local maximum filter decreased commission errors, whereas this process also increased omission errors. When the 10 m radius local maximum filter was applied, we got a large portion of missing trees. Because the window size was too large, tree tops could not be correctly separated. With the 8 m radius filter, we obtained the best accuracy index (33%) among different fixed window-size local maximum filters (Figure 3-8). However, we achieved a better accuracy index (45%) with our method than with the optimized fixed window-size filter (31.7%, when the radius was 8 m), because our method was

more balanced for reducing both omission and commission errors. Because our method applied a progressive window-size filter (from large to small), various sized trees could be correctly detected without the user's intervention. In addition, the geometric characteristics of a canopy profile were examined to reduce false tree top detection. For high trees, we also obtained a better accuracy index (62.8%) with our method than with the optimized fixed window-size filter (46.1%, when the radius was 8 m). For low trees, performance improvement by using our method was limited because low trees did not have distinctive canopy shapes. We expect the accuracy for low trees can be improved by using LiDAR data sets with higher point densities.

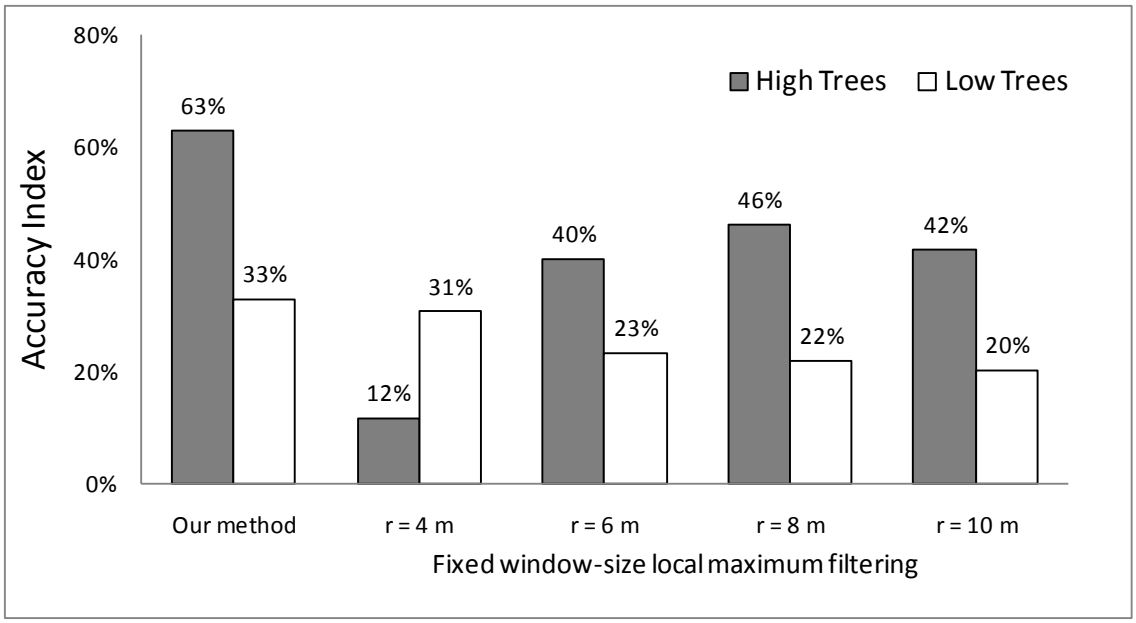

Figure 3-8. Comparison of tree detection and delineation methods by the accuracy index

3.5 Conclusion

In this study, we applied a progressive window-size local maximum filter to detect tree tops from raw LiDAR pulses, followed by the verification of the detected tree tops by the shape of canopy profiles between trees. Then, tree-crown delineation was conducted to separate individual trees. By using the proposed method we were able to correctly detect 65.9% of the reference trees. When we evaluated the accuracy based on crown areas (instead of based on tree counts), we correctly detected 87% of the reference trees in structurally heterogeneous forests. The accuracy index of our method was 81.9%, which was higher than the accuracy index of fixed window-size local maximum filters. Because we used a progressive filter size, we were able to detect a wide range of tree sizes. On the contrary, fixed window-size local maximum filters correctly detected only limited parts of various sizes of trees (depending on the filter size) and were more likely to produce either omission or commission errors. Also, applying additional verification of detected tree tops by using the shape of canopy profiles between trees, we were able to reduced commission errors.

These results showed that the proposed method was able to detect and delineate individual trees in heterogeneous forests using airborne LiDAR data. The delineated trees with the proposed method can be used to extract detailed and precise forest biophysical parameters

(such as tree counts, crown volume, canopy closure, tree height, and biomass) in large forested area in automated manner. Further improvement can be accomplished by increasing the LiDAR pulse density for small trees. Also, more precise species separation will enhance the accuracy of isolating individual trees because we can apply different tree top detection methods, which are selected by the characteristics of trees (both tree species and sizes).

Chapter 4 Combining aerial photographs and LiDAR data with automated tree top detection and registration

4.1 Introduction

As for the quantitative assessment of forest parameters, one of the most promising techniques is light detection and ranging (LiDAR) (Hollaus et al., 2006). There are an increasing number of studies to extract forest biophysical parameters such as tree height, canopy cover, diameter at breast height (DBH), basal area, timber volume, and biomass from LiDAR data (Koch and Dees, 2008; Hyyppä et al., 2008; Lim et al., 2003). LiDAR remote sensing is receiving extensive attention in forest applications because it has the capability of providing both horizontal and vertical information at high spatial resolutions (Hyyppä et al., 2004; Lim et al., 2003). Nonetheless, LiDAR has limited spectral information, which is needed to extract species or health information from the trees. Furthermore, because LiDAR is relatively new, the spatial and historical archives are limited (Baltsavias, 1999).

In contrast, aerial photographs provide spectral information and relatively longer historical archives. Unlike LiDAR, however, it is difficult to acquire accurate 3D forest structural information (such as tree heights) with aerial photography because forest floors are barely visible in dense forest areas (Popescu et al, 2002). Even though the stereo-photogrammetric method can be used to retrieve 3D surface information, automation of the matching is still a difficult task, especially over forested areas, which do not have enough distinctive features (Habib et al., 2005). Given the complementary characteristics of LiDAR and aerial photography, there have been several attempts to combine the two data sets in order to extract forest biophysical characteristics in high spatial resolution. However, the major problem that continues to arise is image registration, particularly when automated (Leckie et al., 2003, McCombs et al., 2003, Suarez et al., 2005). St-Onge et al. (2004) used LiDAR data only for extracting topographic elevation to measure tree height with aerial photographs. Popescu & Wynne (2004) used high spatial resolution CASI imagery to extract land cover information when using LiDAR to estimate tree height. Leckie et al (2003) extracted individual tree information from LiDAR and multi-spectral imagery, but matching between two data sets was not performed. While there has been much research, it is still not easy to combine two data sources at the individual tree level, so the benefit of high spatial resolutions cannot be fully maintained. Holmgren et al. (2008) used a combination of LiDAR data and multi-spectral images for species identification of individual trees, but it required manual registration procedures.

The accurate registration of the photogrammetric and LiDAR data is an essential prerequisite to fully utilize the advantages of both systems (Habib et al., 2005; Schenk and Csathó, 2002). The registration between different datasets requires common features, which are used to geometrically align multiple images. Traditional procedures employ a manual selection of common control points from two datasets for the registration (Habib et al., 2004). However, these manual approaches can be subjective and labor intensive. Also, they may extract only a limited number of usable points with poor spatial distribution so that the overall registration accuracy is reduced (Liu et al., 2006). Automated procedures to extract common features are able to cope with the limitation of manual procedures (Kennedy and Cohen, 2003) There have been various studies about automated image registration techniques (Zitova and Flusser, 2003). In brief, the techniques for identifying control points are categorized into two categories: area-based methods and feature-based methods (Kennedy and Cohen, 2003). Area-based methods

have the advantage of easy implementation and no requirement of pre-processing for the feature extraction. In addition, the resulting control points are evenly distributed over the image so that more robust registration can be performed (Liu et al., 2006; Zitova and Flusser, 2003). However, area-based methods may not be applicable to registering aerial images and LiDAR data because the spatial patterns of pixel grey-scale values (optical reflectance) in aerial images hardly exist in raw LiDAR point data. Conversely, feature-based methods use salient features rather than direct intensity value so that feature-based methods are more suitable for multi-sensor analysis (i.e. LiDAR and aerial images in this study) (Zitova and Flusser, 2003). For feature-based methods, distinctive and detectable common objects (features) should be extracted from both datasets. The common features selected for the registration greatly influence subsequent registration procedures. Hence, it is crucial to decide on the appropriate common features to be used for the registration between the datasets (Habib et al., 2004). Since there is nothing in common at the level of raw data (discrete points in LiDAR and pixels in aerial image), additional processing is required to extract the common features (Schenk and Csathó, 2002). Habib et al. (2005) used linear features for matching. Mitishita et al. (2008) extracted the centroids of rectangular building roofs as common features. Lara Jr. & E.A. Mitishita (2009) proposed corner and edge detection methods for automatic integration of digital aerial images and LiDAR data. However, these methods cannot be applied to non-urban forested areas which do not have built-up objects because these methods require urban objects (e.g. buildings, roads, roofs, etc) for the registration.

Common features for the registration should be distinct, evenly distributed over the entire images, and easily detectable. In forested areas, trees are usually distinctive and spread across the areas so that there is great potential in utilizing distinctive (dominant) trees as control points. Several studies have verified the feasibility of automated tree apex detection in both aerial images and LiDAR data. For aerial images, the studies used the association of a tree top with a local maximum image brightness value (Dralle and Rudemo, 1996; Pouliot et al., 2002; Wulder, 2000). Also, for LiDAR data, there have been extensive studies to detect individual trees by using Digital Surface Model (DSM) from LiDAR data (Chen et al., 2006; Persson et al., 2002; Popescu and Wynne, 2004; Solberg et al., 2006).

The objective of this study is to combine aerial images and LiDAR data by means of automated registration procedures by using tree tops as corresponding control points. More specific aims are: 1) detecting individual tree top locations from LiDAR data and aerial images by using image processing techniques (morphological operation), 2) finding corresponding point pairs between aerial images and LiDAR data, and 3) mosaicking registered multiple aerial images on LiDAR data. The proposed method is specifically designed for structurally heterogeneous forested areas with complex local distortion, which are challenging for automated multi-source data integration at high spatial resolution.

4.2 Study area and remote sensing data

4.2.1 Study Site

This study was conducted at the Angelo Coast Range Reserve (39° 45' N; 123° 38' W; 430-1290 m elevation), part of the University of California Natural Reserve System on the South Fork Eel River in Mendocino County, CA. The Angelo Coast Range Reserve is composed of old conifer forest, dominated by *Pseudotsuga menziesii* (Douglas Fir) and *Sequoia sempervirens* (Redwood) trees (Kotanen, 2004). Elevation ranges from 378 m to 1290 m. Average temperatures range from 16℃ to 31℃ with annual average precipitation of 216 cm/yr (UC Natural Reserve System,

2010). We studied a subset of the larger 180 km^2 of the South Fork Eel river watershed for which LiDAR and aerial photos were acquired by the National Center for Earth-surface Dynamics. Figure 4-1 shows the overview of the subset area by means of the DSM generated from the LiDAR data.

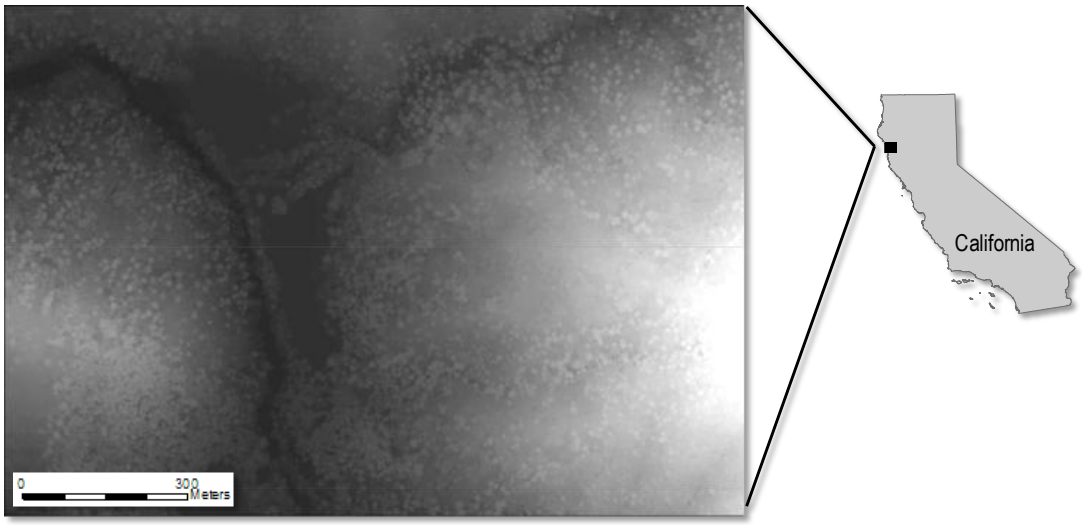

Figure 4-1. Overview of the study area (Digital Surface Model generated from LiDAR data)

4.2.2 Data

Both the LiDAR data and aerial photography were acquired simultaneously on the same airplane on June 29th, 2004. LiDAR data were recorded by the Airborne Laser Swath Mapping (ALSM) system mounted on a Cessna 337 airplane. The ALSM system is comprised of an Optech Inc. model 1233 Airborne Laser Terrain Mapper (ALTM) unit, Inertial Measurement Unit (IMU) and Differential Global Positioning System (DGPS). The laser pulse frequency is 33 kHz, and the swath width is 20 degrees per half angle. The datasets include the first and last pulses for x, y, z coordinates, intensity value, and GPS time. The system acquires 2-3 pulses per 1 m^2 so that the spatial resolution is generally less than 1 m with vertical accuracy of 15-20 cm. Digital aerial images were recorded by an optical 3-Charge-Coupled Device (CCD) digital multispectral camera (Redlake MASD Inc., model MS4100). The resolution is 1920 (H) x 1080 (V) for 2 million pixels with 3 visible bands (R,G,B). The 28 mm focal length lens has a 25 cm x 25 cm spatial resolution at 950 m flying height above ground.

4.3 Methods

The work flow of our method is depicted in Figure 4-2. In this study, we extracted tree tops as common control points from the aerial images and the LiDAR DSM by morphological operations. Then, feature matching between the two data sets was performed to find an initial matching of control points. Because we used point features as control points, we applied a point pattern matching method to find corresponding pairs. In order to cope with radial relief displacement problems in aerial images, only the subset of the detected points (near the principal point) was used for the initial matching. Also, the searching range for the reference points (from the LiDAR DSM) was limited based on camera orientation information such as aerial image center coordinates, flight directions, and flight heights. Once the initial referencing was

conducted, exterior orientation parameters of the aerial image were estimated coarsely. Based on the initial estimation, we iteratively refined exterior orientation by back-projecting tree top locations from LiDAR data onto the aerial images to search and expand corresponding pairs. We rectified aerial images onto LiDAR data by a piecewise-linear transformation with the previously paired control points. After we registered all of each aerial image, adjacent aerial images were combined by means of automatic image mosaicking procedures.

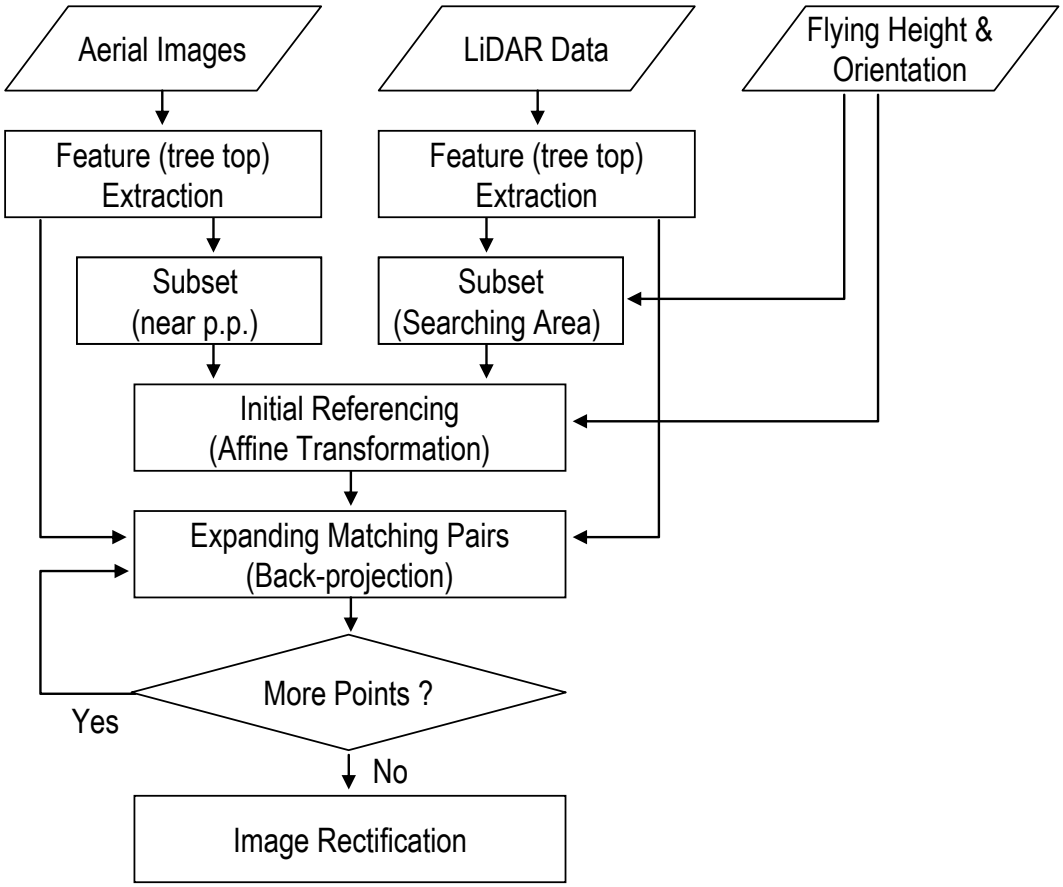

Figure 4-2. Workflow of proposed method

4.3.1 LiDAR Data Analysis

4.3.1.1 Digital Surface Model (DSM)

Tree top detection is typically performed using a canopy height model (CHM), which is calculated by subtracting the DEM from the DSM. However, in this study, we used the DSM rather than the CHM because the DSM is a more realistic representation of canopy surface. In order to detect tree tops by morphological operations, discrete LiDAR points needed to be converted to a regular grid. First, a regular grid was laid out and the maximum elevation point within each cell was assigned as a cell value to derive top vegetation surface (Popescu and Wynne, 2004). Then linear interpolation was performed to create the DSM. The cell size was set to 0.25 m because we intended to process the DSM with aerial photographs which have a spatial resolution of 20 to 30 cm.

4.3.1.2 Smoothing DSM

It is common to smooth the surface before detecting tree tops because smoothing reduces irrelevant surface fluctuations, which can cause inaccurate tree top detection (Wang et al., 2004; Wulder, 2000; Pouliot et al., 2002; Leckie et al., 2005). In this study, we used a 2D Gaussian filter to smooth the DSM. With coarse scales (large smoothing filter sizes), small trees could be missed and overlapping trees could be mistakenly detected as a single tree. In contrast, with fine scales (small smoothing filter sizes), large branches or other variances within a crown could be falsely detected as tree tops. Even though it is impossible to detect all tree tops without any errors by applying just one smoothing parameter, it is required to optimize smoothing parameters for our purpose, which can minimize the number of falsely detected tree tops with enough distance between the points, yet acquire enough correctly detected control points. We used an empirical approach to select an optimum filter size. In this study, it was more important to detect distinctive tree tops rather than not to miss any tree tops. Also, falsely detected tree tops were more problematic than omission errors (missed trees). However, it was required to extract enough tree tops (control points) to construct the accurate transformation equation. Hence, the filter size had to be as small as possible to maximize a number of control points, given that the minimum of the nearest neighbor distances between detected tree tops was larger than the threshold distance. The threshold distance was determined by the searching radius for point matching between the LiDAR data and the aerial images. In order to prevent incorrect control point matching, the distances between the nearest neighbor points are preferred to be larger than the search radius. The search radius was set as 3 meters (12 pixels), Figure 4-3 shows the minimum distance between tree top locations by the different Gaussian filter sizes. We selected 4.75 meters (19 pixels) as the filter size, because the value was the smallest which provided the minimum of neighbor distance which was larger than the threshold value (12 pixels).

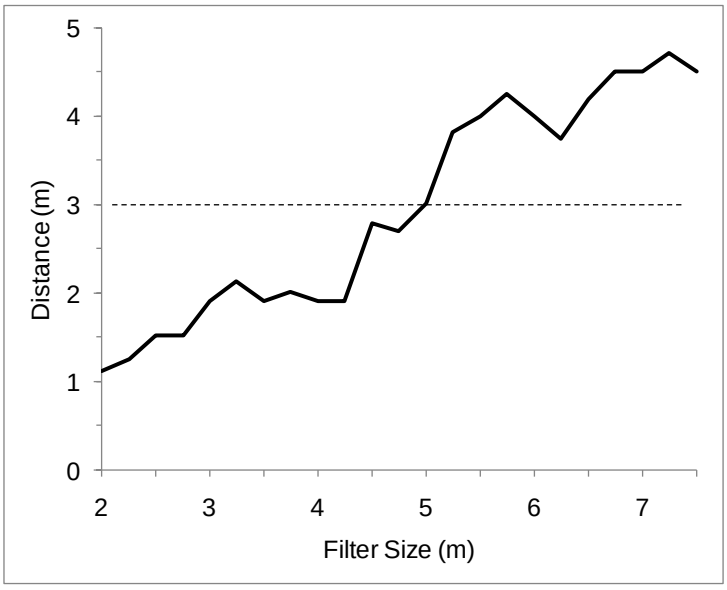

Figure 4-3. The minimum distance between the nearest neighbor tree top points (extracted from the LiDAR data) by different filter sizes

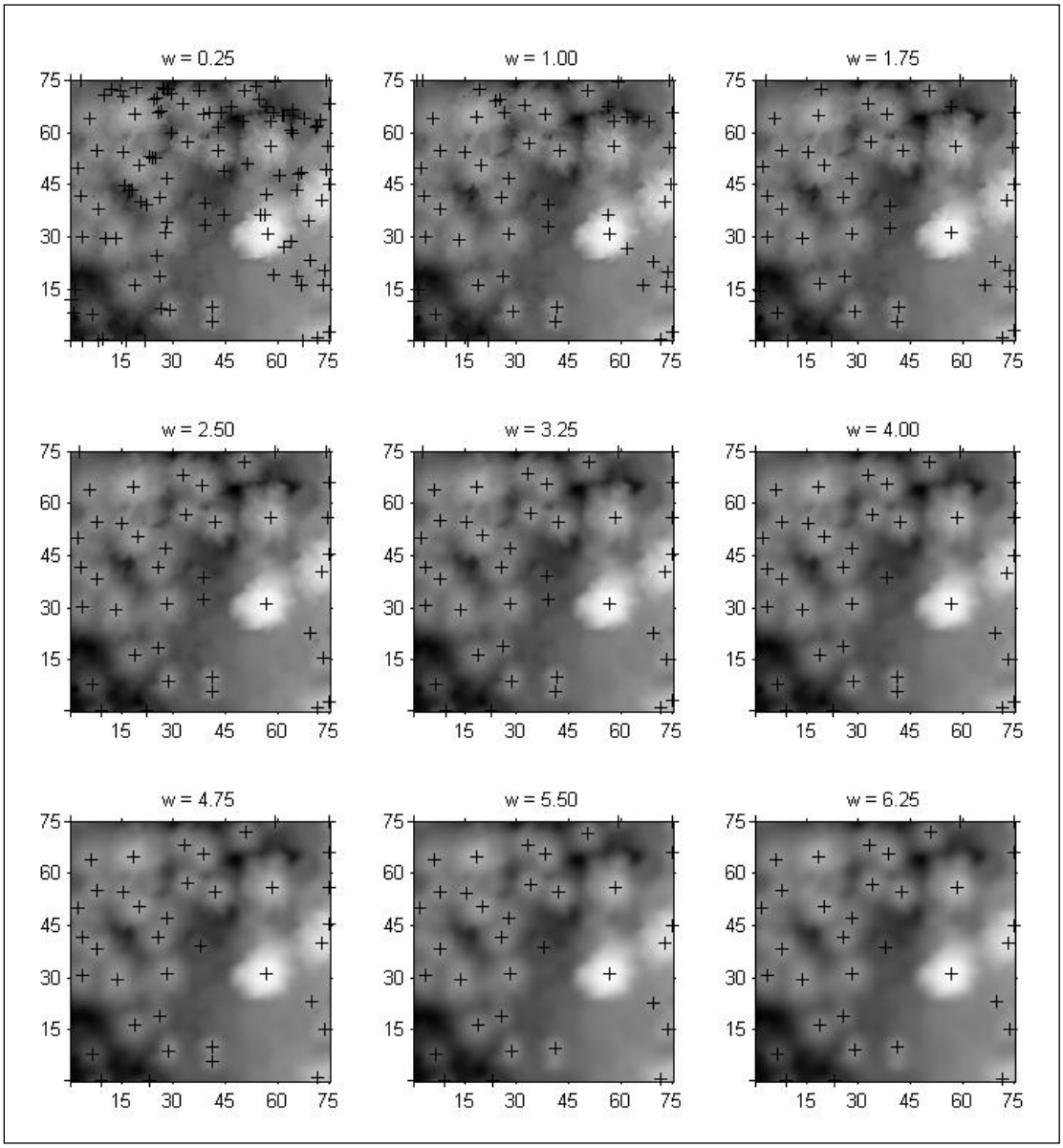

Figure 4-4. An example of the effect of different filter sizes for tree top detection with LiDAR DSM (in meters). *w*: Gaussian filter width

4.3.1.3 Tree top detection by morphological operation with DSM

Extended-maxima transformation, which is the regional maxima of the H-maxima transformation, is a useful method to detect tree tops ("maximal structure") in the canopy surface model (Equation 1).

$$\mathrm{EMAX}_h(f) = \mathrm{RMAX}\left[\mathrm{HMAX}_h(f)\right] \quad (1)$$

The H-maxima transform suppresses all maxima whose depth is lower than or equal to a given threshold level h (Soille, 2003). When it is applied to the DSM, this transformation removes

small fluctuations of the tree canopies, so that the cap of the canopy can be detected by following the regional maxima transformation. The regional maxima transformation identifies "objects", which are higher than their surroundings (Vincent, 1993). In this case, the regional maxima transformation identifies plateaus around tree tops (flattened by the H-maxima transformation) in the canopy surface model. H-maxima transformation is achieved by performing the reconstruction by dilation of f from *f-h* (Equation 2):

$$\mathrm{HMAX}_h(f) = R_f^{\delta}(f - h) \quad (2)$$

The regional maxima transformation is performed by subtracting the dilation of *f-1* from *f* (Equation 3) and this transformation identifies regional maxima as 1 and all others as 0.

$$\mathrm{RMAX}(f) = f + 1 - R_f^{\delta}(f) \quad (3)$$

When the h-value is too small, the results are too sensitive to small fluctuations of the DSM so that the h-value creates too many false tree tops. On the other hand, when the h value is too large, the extended maxima transformation cannot detect tree tops properly. Based on a result from pilot tests, we set the h-value to 1 meter, which was not too sensitive to the fluctuation of DSM and small enough to detect tips of the canopy surface as tree tops. Because the result of extended maxima transformation was a region (connected cells), the point with maximum elevation value in the region was marked as a tree top location.

4.3.2 Aerial Image Analysis

For an individual tree, the tree top is the brightest part because the peak is more likely to be directly illuminated from different sun angles than the edge parts for the convex shape of a tree; adjacent trees will shade the edges of their neighbor (Wulder, 2003). Therefore, reflectance value (image intensity) can represent relative height within an individual tree. The same method as described for extracting individual tree tops from the CHM with the LiDAR data was applied to extract tops of individual trees from aerial images with reflectance values.

4.3.2.1 Grayscale intensity surface

The aerial images, which were used in this study, have three visible bands (red, green, blue). Although multispectral information is useful for object classification, morphological analysis is applicable to only single band images. Accordingly, we converted color images into panchromatic images (intensity) by the "rgb2gray" function in Matlab. Once intensity images were created, these images were processed with the same method we used for the DSM from the LiDAR data.

4.3.2.2 Smoothing aerial images

We applied Gaussian filtering to reduce image noise and remove in-canopy fluctuations (Pouliot et al., 2002). As we did for LiDAR DSM, the optimal smoothing parameters were empirically selected to maximize detecting distinctive tree tops and minimize falsely detected tree tops. Figure 4-5 shows the minimum distance between tree top locations by the different Gaussian filter sizes. We selected 23 pixels as the filter size, because the value was the smallest which provided the minimum of neighbor distance which was larger than a threshold value (12 pixels).

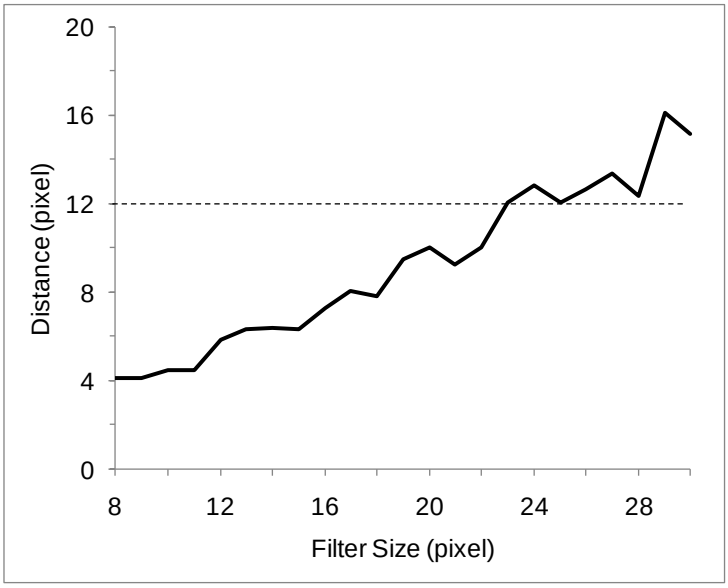

Figure 4-5. The minimum distance between the nearest neighbor tree top points (extracted from the aerial images) by different filter sizes

4.3.2.3 Tree top detection by morphological operation with aerial images

The extended-maxima transformation was applied to identify groups of pixels that represent the tip of tree crowns. Then, the tree apex was detected by selecting the maximum intensity value within a certain group of pixels. An h-value was set to 1 in grayscale images (0 to 255), which was decided by similar pilot tests we did previously. We utilized brightness gradients information to detect tree tops. However, not all of the brighter spots were associated with tree apexes. Thus, we separated vegetation pixels from non-vegetation pixels and excluded non-vegetation pixels because falsely detected tree tops from non-vegetation pixels may cause problems in finding a correct pair of tree tops (as control points). We applied a threshold value for this purpose (Dralle and Rudemo, 1996; Pitkänen, 2001; Pouliot and King, 2005). By using the histogram of brightness values of the detected peak locations, we plotted a histogram and determined the threshold value as 130. Accordingly, only the points, whose pixel value was lower than 130, were classified as tree tops and used as control points.

4.3.3 Initial transformation estimation

Relief displacement increases as the radial distance is increased in aerial photographs (Wolf and Dewitt, 2000). Accordingly, there is only a negligible amount of relief displacement near the principal point so that those parts of the images are close to ortho-rectified images without relief displacement. Because LiDAR data are already geo-rectified with the Differential Global Positioning System (DGPS) and the Inertial Navigation System (INS) system, feature points (tree tops) detected from LiDAR DSM were already geo-registered without any displacement. Tree top point features that were detected from the near principal point in the aerial images have a negligible amount of displacements as well. Hence, a geometric transformation (linear conformal transformation in this study) was applicable to align two sets of points. The major problem to align two data sets was finding correct matching pairs.

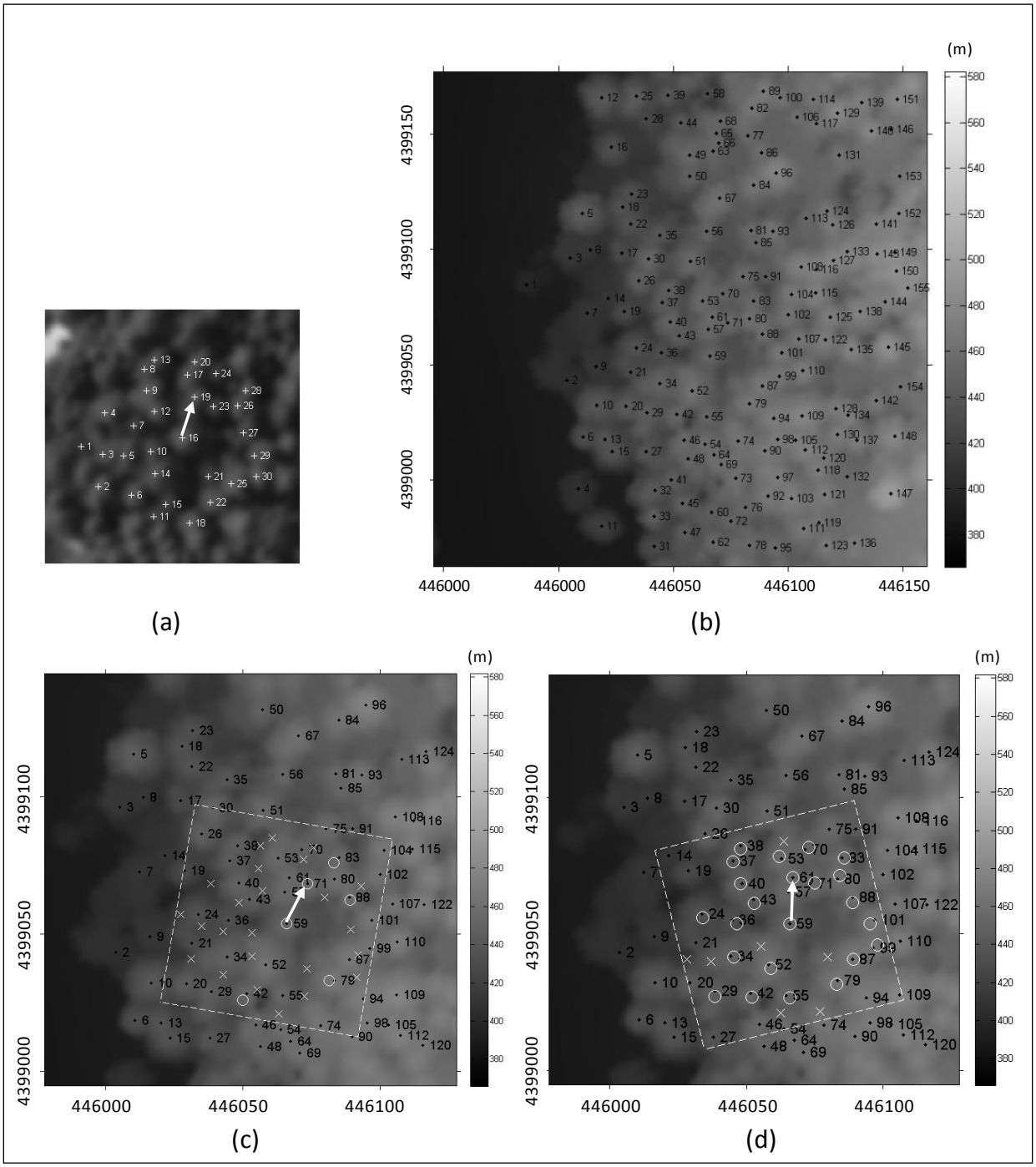

Figure 4-6. An example of initial transformation estimation. (a) Tree tops detected near the center of aerial image (b) tree tops detected from LiDAR DSM (searching area for the matching) (c) an example of incorrect matching (d) an example of correct matching. White circles (O) indicate correctly matched control points, and white crosses (X) indicate incorrectly matched control points. X-axis and Y-axis are coordinates in meters.

In order to solve this problem, we used the fact that the transformation equation estimated from corresponding pairs has the highest number of matching pairs, while the transformation equations from non-corresponding pairs have a limited number of matching pairs. We applied a conformal affine transformation composed of four parameters: s, θ, t_x, and t_y, where s was a scale factor, θ the rotation angle, and t_x and t_y the translation along the x and y directions, respectively. The transformation employed in this step was described by Equation 4.

$$\begin{pmatrix} x_{LiDAR} \\ y_{LiDAR} \end{pmatrix} = \begin{pmatrix} t_x \\ t_y \end{pmatrix} + \begin{pmatrix} s\cos\theta & -s\sin\theta \\ s\sin\theta & s\cos\theta \end{pmatrix} \begin{pmatrix} x_{photo} \\ y_{photo} \end{pmatrix} \quad (4)$$

If the two point pairs are selected from two data sources, transformation parameters (from the aerial images to the LiDAR data) can be estimated. Once the transformation parameters are estimated from the two point pairs, all other points from aerial images are transformed using the transformation equation estimated previously. Then, the nearest point between the two data sources was paired. If the distance between the paired points was within a given threshold (12 pixels), the condition was considered as matching pairs. By using these procedures, all possible point pairs had the count of the correct matching pairs. Then, the pairs with the highest count were selected as corresponding pairs. Figure 4-6 shows an example of the initial transformation estimation. It started with selecting a pair of points (P16 - P19) from the center region of the aerial image (Figure 4-6a). Then, a pair of points was selected from the LiDAR data (Figure 4-6b). Figure 4-6c shows an example of an incorrect matching. When an incorrect pair of points (P59 - P71) was selected from the LiDAR data, the transformation provided small number of matching points (5 cases in this example). Conversely, when the correct pair of points (P59 - P61), we acquired the highest number of matching pairs (23 cases in this example) (Figure 4-6d).

In order to speed up the search procedure, we reduced the search sets by setting up threshold values for transformation angles and scales. The point pairs which are out of the range of the threshold values were excluded when finding matching pairs. Also, these threshold values helped to prevent false corresponding pairs. The angle thresholds were calculated from the flight line data. The flight line data had the approximate orientation of each image so that the angle thresholds are set to the flight line orientation angle ± 5 degrees. The scale threshold is estimated from the average flight height. The range of threshold height was set to ± 200 m of the average flight height. Then, the scale threshold range was calculated from the focal length and the average flight height. We intended to expand the threshold value of the orientation angle and the scale, but we were able to find the corresponding point pairs using the initial threshold values. Therefore, we did not need to expand threshold values.

4.3.4 Iterative matching point expansion and exterior orientation refinement

Although we used geometric relations of the points between the two data sets for finding corresponding pairs between aerial images and LiDAR DSM for initial matching, this approach was only applicable to a limited part of the image (near the principal point). As the radial distance increased, the relief displacement was increased, and the geometric relations of points were not consistent. Consequently, it was necessary to consider relief displacement of aerial images for finding corresponding pairs by the nearest point matching scheme (the nearest points between two data sources were paired if the distance between two points was smaller than a threshold value). Because the feature points from the LiDAR data had 3D information (x,y,z)

and the external orientation parameters were already estimated from the previous steps, we were able to apply the backward projection of 3D feature points from the LiDAR DSM (in object space) into the aerial images (in image space) for searching and adding corresponding pairs. The backward projection was conducted using the collinearity equation (Equation 5)

$$\begin{cases} x = x_0 - f \cdot \dfrac{r_{11}(X - X_c) + r_{12}(Y - Y_c) + r_{13}(Z - Z_c)}{r_{31}(X - X_c) + r_{32}(Y - Y_c) + r_{33}(Z - Z_c)} \\ y = y_0 - f \cdot \dfrac{r_{21}(X - X_c) + r_{22}(Y - Y_c) + r_{23}(Z - Z_c)}{r_{31}(X - X_c) + r_{32}(Y - Y_c) + r_{33}(Z - Z_c)} \end{cases} \quad (5)$$

where X_c, Y_c, and Z_c, were ground coordinates of the camera location, and x_0 and y_0 were image coordinate of the principal point. f was the camera focal length, and r_{11}, r_{12}, … r_{33} were the camera orientation parameters estimated from the previous steps.

Once we performed the backward projection, the nearest point matching scheme could be used to find corresponding pairs between the two data sets. Based on newly added control point pairs, external orientation parameters were updated and used for the next step. At each step, the radius (a distance from the principal point) of the search area is gradually increased until all the points in the image were used.

4.3.5 Image rectification

Once the feature corresponding between the LiDAR data (reference) and the aerial images was established, the mapping function should be determined for the image registration (Zitova and Flusser, 2003). In order to establish the mapping function, the type of the mapping function needs to be selected and the parameters for the function should be estimated. Models of mapping functions can be divided into two broad groups; global and local transformation models. For global transformation models, the model parameters are the same for the entire image so that they are inappropriate to handle various local distortions. In contrast, local transformation models can have different model parameters, which depict local distortions across the whole image (Zitova and Flusser, 2003). Because the aerial images are acquired over the heterogeneous mixed forests that consist of tall conifer trees and steep topographic slopes, the aerial images have various local geometric distortions. Thus, in this study, we employed a local transformation model to determine the mapping function. More specifically, we applied a piecewise linear mapping, which decomposes the whole image into triangular facets, and then used local mapping functions to model the local geometric distortions (Goshtasby, 1986; Liu et al., 2006). We constructed a Delaunay triangulation to decompose the input image by using the extracted control points, and we rectified the image by estimating the transformation of each triangular facet. In addition, we employed three global transformation models (affine, 2nd, and 3rd) for the purpose of comparison.

4.3.6 Multi-frame mosaicking

Mosaicking combines several image frames into a single composite image to cover a large area (Kerschner, 2001). Aerial photographs are a common source for creating photo mosaics because multiple frames are acquired to cover a large area (Afek and Brand, 1998). Because we rectify multi-frame images, which cover a part of the study area, we also perform image mosaicking to

combine the rectified aerial images. In mosaicking two adjacent images, it is necessary to decide how to process the overlapping areas. In most cases, a seam line (cutline) is defined between two images and the overlapping regions are blended to create a seamless mosaic (Afek and Brand, 1998). In this study, we decomposed each frame into triangular facets which was constructed by the common control points. Accordingly, each triangle facet had different transformation functions based on the control points. Then, the whole mapping function was acquired by piecing triangular regions together. Because the image mosaicking combined multiple images into one large image, adjacent image frames had overlapping areas. We used the proximity of the triangular facet to the center of the images in order to determine which image frame would be selected for each triangular region. The proximity was calculated by finding the nearest image center point from the vertices of the triangle.

4.3.7 Evaluation of the image registration accuracy

For evaluating the accuracy of the registration, we applied the Leave-One-Out Cross-Validation (LOOCV), which is a common cross-validation method. Cross-validation is a statistical method of evaluating and comparing the performance of learning algorithms by dividing data into two groups (one is for learning or training, and the other is for validation (Stone, 1974). The LOOCV is a special case of the k-fold cross-validation method, which split the data into k mutually exclusive subsets of equal (or almost equal) size (Kohavi, 1995). In k-fold cross-validation, a single subset is retained for validation, and the remaining k-1 subsets are used as training data. The training and validation are performed iteratively (k times) so that each of the k subsets is used exactly once (Refaeilzadeh and Tang, 2009). The LOOCV uses only one observation for validation and uses the remaining observations as training data. In other words, the LOOCV is a k-fold cross validation, where k is equal to the size of the dataset. Accordingly, we retained one control point from the pool as a validation point and estimated a geometric transformation function using the remaining points. Then, we applied this transformation function to locate the retained control point. In each iteration, we calculated the residual (distance) between the true point and the estimated point. By using the calculated residuals, we calculated the maximum x-residual, the maximum y-residual, the total RMSE, the median absolute deviation (MAD), and the standard deviation (SD) of the residuals to evaluate the registration errors. Also, we used these indexes to compare the differences between transformation models (affine, 2^{nd} polynomial, 3^{rd} polynomial, and piecewise linear model).

4.4. Results and Discussions

4.4.1 Tree top detection and matching

Table 4-1 shows the number of feature points extracted from aerial images and LiDAR data in the initial matching step. In this study, the aerial images had more feature points than the LiDAR data. Accordingly, the matching points between two data sets were mainly limited by the feature points obtained from the LiDAR data. Although some images had fewer corresponding points than the others, all the images had enough control points to estimate initial exterior orientation parameters. Table 4-2 lists the number of feature points obtained in automatic tree top detection from both data sets and the number of corresponding points by iterative matching point expansion. On average, we detected 1038 feature points from each aerial image, and we detected 394 points from the LiDAR data from the equivalent area. Overall, 80 percent of the feature points from the LiDAR data were matched to corresponding points for the transformation.

However, only 30.5% of the feature points from the aerial images were paired with the corresponding points from the LiDAR data. This was mainly because small deciduous trees had less distinctive apexes in the canopy. Consequently, those fluctuations were removed by strong low pass filtering.

Table 4-1. Numbers of detected feature points and matched points (initial matching)

Image	Feature extraction		Matching points		
number	Aerial Image	LiDAR	n	m/A	m/L
7552	30	26	25	83.3%	96.2%
7553	34	19	16	47.1%	84.2%
7554	27	18	16	59.3%	88.9%
7732	33	14	14	42.4%	100.0%
7733	22	15	13	59.1%	86.7%
7734	33	14	13	39.4%	92.9%
Total	179	106	97	54.2%	91.5%

* m/A: number of matched point / number of feature points from aerial images, m/L: number of matched point / number of feature points from LiDAR data

Table 4-2. Numbers of detected feature points and matched points (final matching)

Image	Feature extraction		Matching points		
number	Aerial Image	LiDAR	n	m/A	m/L
7552	1135	468	414	36.5%	88.5%
7553	1111	450	384	34.6%	85.3%
7554	1106	486	387	35.0%	79.6%
7732	1016	356	201	19.8%	56.5%
7733	947	306	276	29.1%	90.2%
7734	917	296	239	26.1%	80.7%
Total	6232	2362	1901	30.5%	80.5%

* m/A: number of matched point / number of feature points from aerial images, m/L: number of matched point / number of feature points from LiDAR data

4.4.2 Transformation model comparison

We applied a local transformation model (piecewise linear model) to register the aerial images to the LiDAR data. In addition, we used three global transformation models (affine, 2^{nd} polynomial, and 3^{rd} polynomial) for the purpose of comparison. We employed the LOOCV method to evaluate the accuracy of the registration between the aerial images and LiDAR data. Table 4-3 shows the result of accuracy assessment by using four different registration error indexes: maximum x-residual, maximum y-residual, total RMSE, and MAD. All the registration error

indexes verify that the piecewise linear model produced the smallest registration errors. Because a global transformation model cannot properly handle local image deformation, a global transformation model has relatively larger registration errors than a local transformation model. Therefore, when we applied a piecewise linear model, the total RMSE of the residual was 9.21 pixels (2.3 meters), and MAD was 6.81 pixels (1.41 meters). The maximum X directional errors were larger than the maximum Y directional errors, because the aerial images were wider in the X (1920 pixels) direction than in the Y direction (1080 pixels). As the distance from the principal point increased, the relief displacement also increased. Therefore, it was more likely to have a larger number of points which were further away from the principal point in the X direction than in the Y direction.

Table 4-3. Comparison between models and accuracy indexes (in meters)

Transformation Model	Max X Residual	Max Y Residual	Total RMSE	MAD	S.D. of the residual
Affine	15.08	13.51	4.88	3.77	2.42
2nd Polynomial	13.33	8.54	2.94	1.87	1.78
3rd Polynomial	11.65	8.05	2.48	1.70	1.42
Piecewise Linear	10.12	6.27	2.30	1.41	1.41

4.4.3 Image mosaicking

We mosaicked six overlapping images into one by using common control points which were shared by adjacent images. We visually examined the transitional areas between images for comparisons. Compared to the outcome of the simple proximity based image mosaicking method, the result of our method showed seamless transitions around the seam lines (Figure 4-8). The quality of the seamless transition between images was better when enough common control points existed. However, when the overlapping area had sparse common points, the seam lines were more noticeable because of misalignment between the neighboring images. In this study, the test site included the open areas without trees. Thus, these open areas have sparsely distributed control points so that the transitions between the images around the open areas were less smooth than the transitions between the images around the densely forested areas.

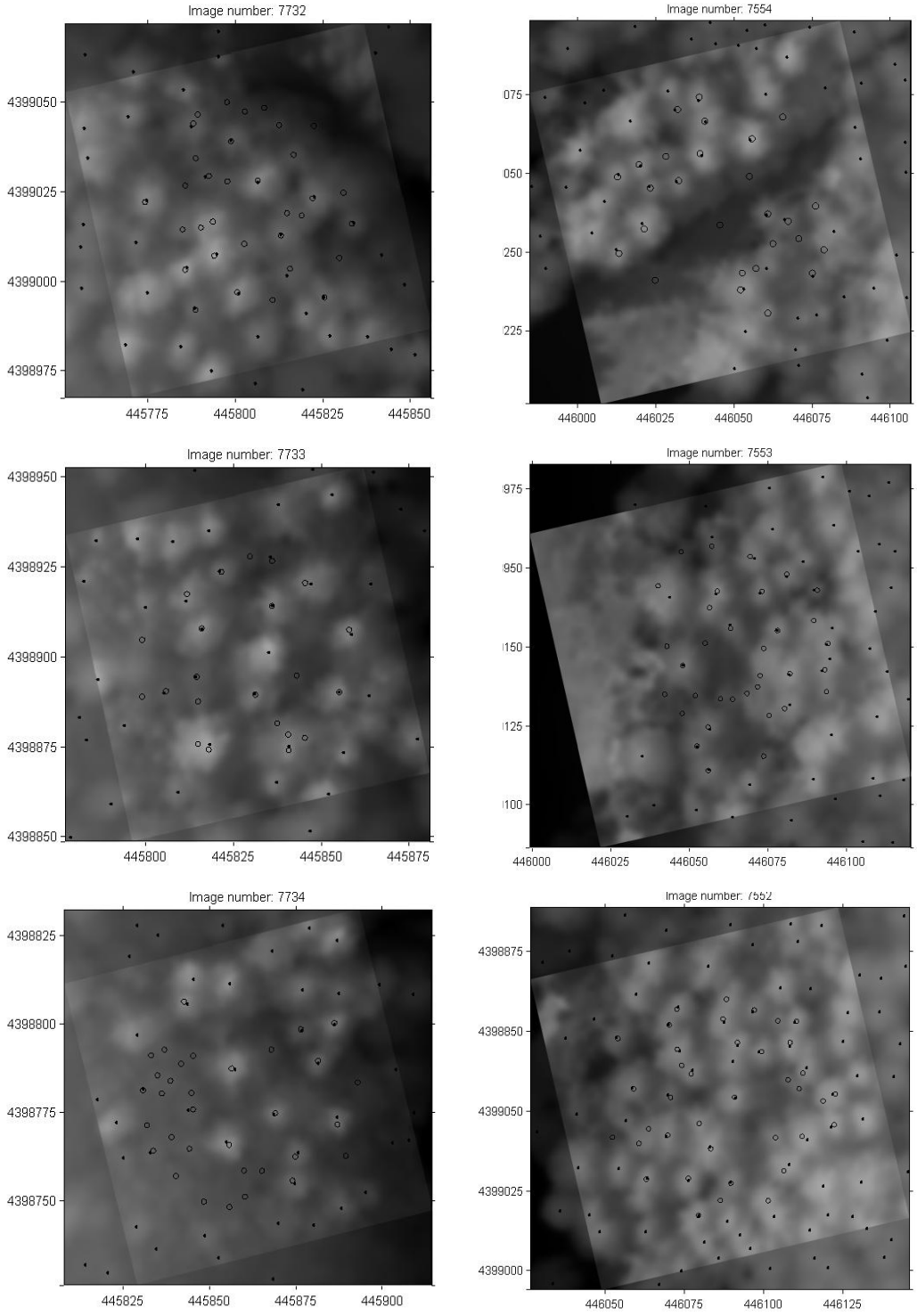

Figure 4-7. The result of initial registration of aerial images with LiDAR DSM. Aerial images are overlaid on LiDAR DSM. (○): Tree tops from aerial images, (•): tree tops from LiDAR DSM. X-axis and Y-axis are coordinates in meters

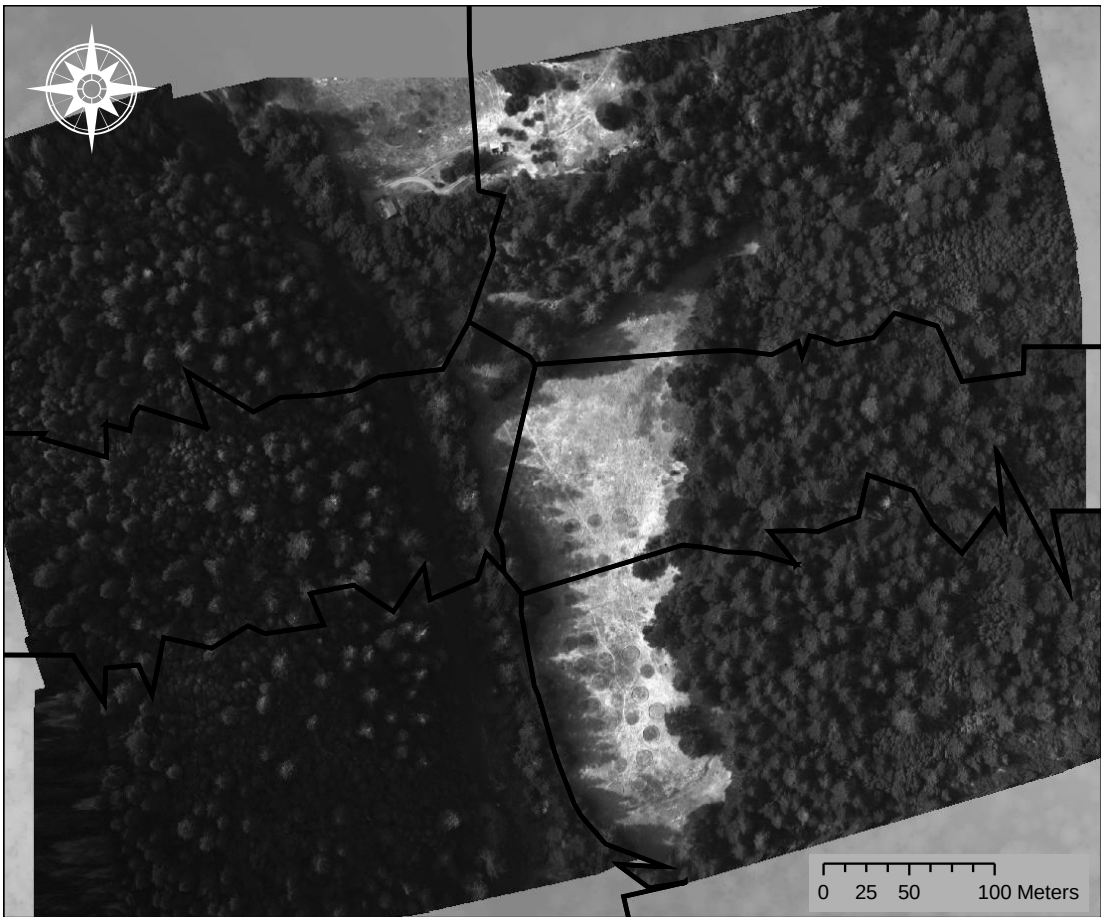

Figure 4-8. Result of the mosaicked aerial image. Lines indicates seam lines between aerial images

4.5 Discussion

Automatic registration of multi-source remote sensing is not an easy task because it needs to handle various radiometric characteristics, image resolution, sensor orientation, and local deformation in the registration procedures: feature identification, feature matching, spatial transformation, and interpolation (Zitova and Flusser, 2003). Combining multi-spectral images and LiDAR data is useful because the complementary characteristics of LiDAR and aerial photography enable us to fully utilize the advantages of both systems (Habib et al., 2005; Schenk and Csathó, 2002) . However, these multi-source data sets have very different radiometric characteristics, so that it is challenging to identify and match common corresponding features to register the two data sets by automated procedures. In this study, we employed trees, which are abundant over forested areas, as common control points for the feature-based registration. In addition, we utilized the geometric distribution (or constellation) of the detected tree tops to find initial corresponding point pairs to cope with the difficulty of finding corresponding pairs between the aerial images and the LiDAR data, which had very different radiometric characteristics. The results indicated that tree tops were able to be used to register high spatial resolution multi-source remote sensing data in forested areas. Also, as we expected, the piecewise linear transformation was more accurate than other polynomial and affine

transformation methods. However, the accuracy differences between the piecewise linear transformation and other polynomial transformation methods were less distinctive than our expectation. We suspect some regions do not have enough control points for the accurate registration and this problem might diminish the advantage of using a local transformation method, which can reflect various localized geometric distortions, over global transformation methods. It is worth mentioning that this problem is directly related to the limitations of the proposed method.

We applied Gaussian filtering on the aerial images and the LiDAR data to detect only distinctive tree tops. We dismissed small trees by applying relatively strong smoothing on the images to prevent false matching between two data sets. As we previously explained, we determined the Gaussian filter size to ensure enough distances between the nearest neighbor points. Because the filter size was mainly optimized to minimize false matching between control points, relatively small trees, which had the potential to be served as feature points, were not able to be detected and used for the registration procedures. Consequently, in the regions dominated by small trees, our method detected and matched only a limited number of feature points, so that the accuracy of the registration diminished. This limitation suggested to us that variable filter size can be implemented to improve tree top delectability so that small trees contribute to the improvement of registration accuracies

As we mentioned before, our method is intended to be used mainly for forested areas, which do not have commonly used distinctive features (such as buildings, roads, roofs, etc). Hence, we use tree tops as common feature points to register the aerial images to LiDAR data. However, we expect that it may be difficult to find feature points in areas with no trees so that the accuracy of the registration will be decreased in those areas. Furthermore, because initial matching between the aerial images and the LiDAR data is conducted around the center of the aerial images, the initial matching might encounter problems when the center of the aerial image does not have any trees. Consequently, the following iterative matching point expansion might not be able to be conducted correctly. Although we do not have this problem from the 6 test images, we need to consider the possibility of this problem and to improve our method in future research.

In this study, we acquired the aerial images by a non-calibrated, non-metric digital camera. Hence, the interior orientation information was not included in the backward projection for the control point expansion steps. Because we did not perform any analytical photogrammetric measurements, omitting the interior did not cause any critical problems on our registration procedures. However, we expected that including interior orientation information would improve the accuracy of the image registration results.

4.6 Conclusion

In this study, we proposed an approach for automatic registration of aerial images with LiDAR data. We started from extracting tree tops as common feature points from both data sets by applying a morphological operation (extended-maxima transformation). Then, we conducted the preliminary matching by using the small region of the image center, which was near the principal point. Because we intended to search corresponding points between two data sets by using only geometric distribution of the control points, we initially used only a small region near the image center, which did not have relief displacement problems. We iteratively expanded the control points to the entire images by using the backward projection of the tree top points of the LiDAR data over the aerial images. The backward projection was performed based on the exterior

orientation parameters estimated from the previous step and corresponding points were paired by the nearest neighbor searching method. Once the corresponding point pairs were found, the transformation function was estimated to register the aerial images to the LiDAR data. We compared a local transformation method and global transformation method. The evaluation of the accuracy was performed by the LOOCV method. A local transformation method (piecewise linear transformation) provided us better registration accuracy than the other global transformation methods (affine, 2^{nd} polynomial, and 3^{rd} polynomial transformation). Finally, we mosaicked the previously geo-rectified aerial images into one large image. The seam lines were selected using the triangulation of common control points between adjacent images. Although the adjacent triangles had different transformation functions, the discrepancies between the images on the shared border lines were hardly noticeable, because the border line shared two common control points (both end points of the line) between two images. Our approach of the image mosaicking was fully automated in searching for the seam lines and combining multiple images. Consequently, we were able to acquire a qualitative image mosaic from the multiple aerial images.

The main limitation of our approach was to use only tree tops as matching feature points for the registration. Although our approach performed well over the forested area with enough distinctive trees, it would be very difficult to register the aerial images with LiDAR data over an area with no detectable trees. We need more efforts to include other corresponding features (other than tree tops) to cope with this problem for future studies.

We expect the proposed approach will enable us to integrate aerial images and LiDAR data at the individual tree level. Hence, the integrated data sets may serve to extract detailed forest biophysical parameters so that more detailed and accurate information will help to expand our understanding of forest ecosystem dynamics.

Chapter 5 Conclusions

In this dissertation, three important topics, related to extracting individual tree level biophysical parameters by using high spatial resolution remotely sensed data, were studied. Although the potential of using high spatial resolution data to extract detailed forest inventory parameters were substantial, they could be realized only if we employed adequate methods for extracting detailed information inherent in the LiDAR and aerial imagery. Accordingly, I developed and evaluated new approaches for three different topics related to this objective: 1) classifying raw LiDAR points into ground and non-ground points, 2) detecting tree tops and delineating an individual tree crown, and 3) combining aerial images and LiDAR data by means of automated registration procedures.

Classifying raw LiDAR points (ground vs. non-ground) for generating a terrain surface is a basis for other analysis related to forest biophysical parameter extraction. In Chapter 2, I developed the Progressive Terrain Fragmentation (PTF) method to improve the performance of filtering non-terrain points from raw airborne laser scanning data. Iterative procedures for searching terrain points gradually approximates terrain surface. Instead of using absolute slope or offset distance, this method utilizes orthogonal distance to and relative angle between a triangular plane and a node. For that reason, PTF was able to classify raw LiDAR points into ground and non-ground points on a heterogeneous steep forested area with a small number of parameters. I found an angle threshold to be the most influential parameter for accurate filtering procedures. I also found a smaller angle threshold causes inaccurate terrain approximation by omitting terrain points around ridge lines. Conversely, a large angle threshold failed to remove low vegetation. The optimum threshold value was determined by examining reference plots in the study site, and the selected threshold value was applied for the entire level of filtering procedures. However, the result of the accuracy assessment indicated the accuracies were vary depend on the site conditions (e.g. tall vegetation vs. low shrubs). Accordingly, in future work these methods should be tested under different environmental conditions.

Detecting and delineating individual tree crowns is an important prerequisite in extracting various forest inventory parameters from high spatial resolution data. In Chapter 3, I developed an automated method to detect individual tree tops and delineate individual tree-crown boundaries using airborne LiDAR data. I applied a progressive window-size local maximum filter to detect tree tops from raw LiDAR pulses, followed by the verification of the detected tree tops by the shape of canopy profiles between trees so that I was able to improve the accuracy of tree top detection by reducing commission errors. Then, tree-crown delineation was conducted to separate individual trees. Further improvement can be accomplished by increasing the LiDAR pulse density for small trees. Also, more precise species separation will enhance the accuracy of isolating individual trees because we can apply different tree top detection methods, which are selected by the characteristics of trees (both tree species and sizes).

In Chapter 4, I proposed a new approach for automatic registration of aerial images with LiDAR data. I employed trees, which were abundant over forested areas, as common control points for the feature-based registration. In addition, I utilized the geometric distribution (or constellation) of the detected tree tops to find initial corresponding point pairs to cope with the difficulty of finding corresponding pairs between the aerial images and the LiDAR data, which had very different radiometric characteristics. The results indicated that tree tops were able to be used to register high spatial resolution, multi-source remote sensing data in forested areas. In

addition, the piecewise linear transformation was more accurate than other polynomial and affine transformation methods. The geo-registered images were combined into one large image by using common control points between adjacent images so that a qualitative image mosaic was able to be acquired. The main limitation of this approach was to use only tree tops as matching feature points for the registration. Although this approach performed well over the forested area with enough distinctive trees, it would be very difficult to register the aerial images with LiDAR data over an area with no detectable trees. Further study is needed to include other corresponding features (other than tree tops) to cope with this problem.

Future implications

The results from this dissertation can be used as the foundation for further research on extracting various forest biophysical parameters. In Chapter 2, I separated raw LiDAR points into ground returns and non-ground returns. The LiDAR points, which were classified as ground returns by PTF method, were initially used to reconstruct the terrain surface model. Because tree heights are obtained by subtracting a digital terrain model from a canopy surface model, reconstructing an accurate terrain model will contribute to accurate estimation of tree height in forested areas. Although non-ground return points were filtered out for reconstructing the ground surface model, those non-ground return points can be used to extract other forest biophysical characteristics related to tree canopies. For example, Leaf Area Index (LAI) can be estimated by the ratio between total returns (ground returns + canopy returns) and canopy returns. In addition, the distribution of non-ground returns (canopy returns) can be used to determine the tree species. In Chapter 3, I detected and delineated individual trees in heterogeneous forests using airborne LiDAR data. Because obtaining forest biophysical measurements from the LiDAR data require an object from which to extract those measurements, it is effective to use individual trees as an object for this purpose. For example, tree height and crown diameter can be extracted only if the boundaries of individual trees are delineated. Then, indirect forest inventory variables, such as diameter at breast height (DBH), basal area, stem volume, and biomass can be estimated. Furthermore, detailed individual tree measurements can be used for developing and calibrating forest ecosystem models. In Chapter 4, I integrated aerial images and airborne LiDAR data by the feature-based automatic registration procedures. Because the spectral information from aerial images provides complementary information, which cannot be acquired by only LiDAR data, combining aerial images and LiDAR data may improve our ability to extract forest information. In particular, this work can improve the classification of tree species by providing additional spectral information. In addition, I expect that multi-temporal aerial images can be co-registered so that the proposed method might be applicable to change detection and retrospective analysis for forest ecosystems.

References

Afek, Y., and Brand, A. (1998). Mosaicking of orthorectified aerial images. Photogrammetric Engineering and Remote Sensing *64*, 115–124.

Andersen, H. E., Reutebuch, S. E., and Schreuder, G. F. (2001). Automated individual tree measurement through morphological analysis of a LIDAR-based canopy surface model. Precision Forestry, 11.

Axelsson, P. (2000). DEM generation from laser scanner data using adaptive TIN models. International Archives of Photogrammetry and Remote Sensing *33*, 111–118.

Baltsavias, E. (1999). A comparison between photogrammetry and laser scanning. ISPRS Journal of Photogrammetry and Remote Sensing *54*, 83-94.

Bater, C. W., and Coops, N. C. (2009). Evaluating error associated with lidar-derived DEM interpolation. Comput. Geosci. *35*, 289-300.

Brandtberg, T. (1999). Remote sensing for forestry applications - a historical retrospect. Available at: http://homepages.inf.ed.ac.uk/rbf/CVonline/LOCAL_COPIES/BRANDTBERG/UK.html [Accessed January 19, 2010].

Chen, Q., Baldocchi, D., Gong, P., and Kelly, M. (2006). Isolating individual trees in a Savanna woodland using small footprint lidar data. Photogrammetric Engineering and Remote Sensing *72*, 923–932.

Chen, Q., Gong, P., Baldocchi, D., and Xie, G. (2007). Filtering airborne laser scanning data with morphological methods. Photogrammetric Engineering and Remote Sensing *73*, 175.

Clark, M. L., Clark, D. B., and Roberts, D. A. (2004). Small-footprint lidar estimation of sub-canopy elevation and tree height in a tropical rain forest landscape. Remote Sensing of Environment *91*, 68–89.

Cobby, D. M., Mason, D. C., and Davenport, I. J. (2001). Image processing of airborne scanning laser altimetry data for improved river flood modelling. ISPRS Journal of Photogrammetry and Remote Sensing *56*, 121–138.

Culvenor, D. S. (2003). Extracting individual tree information. In Remote Sensing of Forest Environments: Concepts and Case Studies, pp. 255–277.

Dale, V. H., Joyce, L. A., McNulty, S., Neilson, R. P., Ayres, M. P., Flannigan, M. D., Hanson, P. J., Irland, L. C., Lugo, A. E., Peterson, C. J., et al. (2001). Climate Change and Forest Disturbances. BioScience *51*, 723-734.

Davenport, I., Holden, N., and Gurney, R. (2004). Characterizing errors in airborne laser altimetry data to extract soil roughness. Geoscience and Remote Sensing, IEEE Transactions on *42*, 2130-2141.

Dralle, K., and Rudemo, M. (1996). Stem number estimation by kernel smoothing of aerial photos. Canadian Journal of Forest Research *26*, 1228–1236.

Evans, J. S., and Hudak, A. T. (2007). A multiscale curvature algorithm for classifying discrete return lidar in forested environments. IEEE Transactions on Geoscience and Remote Sensing *45*, 1029–1038.

Fensham, R. J., and Fairfax, R. J. (2002). Aerial photography for assessing vegetation change: a review of applications and the relevance of findings for Australian vegetation history. Australian Journal of Botany *50*, 415–429.

Franklin, S. (2001). Remote sensing for sustainable forest management (Boca Raton Fla.: Lewis).

Goshtasby, A. (1986). Piecewise linear mapping functions for image registration. Pattern Recognition *19*, 459–466.

Habib, A., Ghanma, M., and Mitishita, E. (2004). Co-registration of photogrammetric and LIDAR data: Methodology and case study. Revista Brasileira de Cartografia *56*, 1–13.

Habib, A., Ghanma, M., Mitishita, E., and Kim, E. (2005). Image georeferencing using LIDAR data. In Geoscience and Remote Sensing Symposium, 2005. IGARSS '05. Proceedings. 2005 IEEE International, pp. 1158-1161.

Hall, R. J. (2003). The roles of aerial photographs in forestry remote sensing image analysis. Remote Sensing of Forest Environments: Concepts and Case Studies, 47–75.

Hodgson, M. E., and Bresnahan, P. (2004). Accuracy of airborne lidar-derived elevation: empirical assessment and error budget. Photogrammetric engineering and remote sensing *70*, 331–340.

Hollaus, M., Wagner, W., Eberhofer, C., and Karel, W. (2006). Accuracy of large-scale canopy heights derived from LiDAR data under operational constraints in a complex alpine environment. ISPRS Journal of Photogrammetry and Remote Sensing *60*, 323-338.

Holmgren, J., Persson, Å ., and Söderman, U. (2008). Species identification of individual trees by combining high resolution LiDAR data with multi-spectral images. International Journal of Remote Sensing *29*, 1537-1552.

Holmgren, J. (2004). Prediction of tree height, basal area and stem volume in forest stands using airborne laser scanning. Scandinavian Journal of Forest Research *19*, 543-553.

Houghton, J. T., Ding, Y., Griggs, D. J., Noguer, M., van der Linden, P. J., Dai, X., Maskell, K., and Johnson, C. A. (2001). Climate change 2001: the scientific basis (Cambridge University Press Cambridge).

Hunter, J. C., and Barbour, M. G. (2001). Through-Growth by Pseudotsuga menziesii: A Mechanism for Change in Forest Composition without Canopy Gaps. Journal of Vegetation Science *12*, 445-452.

Hyyppä, J., Hyyppä, H., Leckie, D., Gougeon, F., Yu, X., and Maltamo, M. (2008). Review of methods of small-footprint airborne laser scanning for extracting forest inventory data in boreal forests. Int. J. of Remote Sensing *29*, 1339-1366.

Hyyppä, J., Hyyppä, H., Litkey, P., Yu, X., Haggrén, H., Rönnholm, P., Pyysalo, U., Pitkänen, J., and Maltamo, M. (2004). Algorithms and methods of airborne laser-scanning for forest measurements. International Archives of Photogrammetry, Remote Sensing and Spatial Information Sciences *36*, 1682–1750.

Kadmon, R., and Harari-Kremer, R. (1999). Studying long-term vegetation dynamics using digital processing of historical aerial photographs. Remote Sensing of Environment *68*, 164–176.

Kennedy, R. E., and Cohen, W. B. (2003). Automated designation of tie-points for image-to-image coregistration. International Journal of Remote Sensing *24*, 3467-3490.

Kerschner, M. (2001). Seamline detection in colour orthoimage mosaicking by use of twin snakes. ISPRS Journal of Photogrammetry and Remote Sensing *56*, 53–64.

Kilian, J., Haala, N., and Englich, M. (1996). Capture and evaluation of airborne laser scanner data. In International Archives of Photogrammetry and Remote Sensing, Vol. XXXI, Part B3 (Vienna, Austria), pp. 383-388.

Kobler, A., Pfeifer, N., Ogrinc, P., Todorovski, L., Ostir, K., and Dzeroski, S. (2007). Repetitive interpolation: A robust algorithm for DTM generation from Aerial Laser Scanner Data in forested terrain. Remote Sensing of Environment *108*, 9–23.

Koch, B., and Dees, M. (2008). Forestry applications. In Advances in Photogrammetry, Remote Sensing and Spatial Information Science: 2008 ISPRS Congress Book, pp. 439–465.

Koch, B., Heyder, U., and Weinacker, H. (2006). Detection of individual tree crowns in airborne lidar data. Photogrammetric Engineering and Remote Sensing *72*, 357.

Kohavi, R. (1995). A study of cross-validation and bootstrap for accuracy estimation and model selection. In International joint Conference on artificial intelligence, pp. 1137–1145.

Kotanen, P. M. (2004). Revegetation following soil disturbance and invasion in a Californian

meadow: a 10-year history of recovery. Biological Invasions *6*, 245–254.

Kraus, K., and Pfeifer, N. (1998). Determination of terrain models in wooded areas with airborne laser scanner data. ISPRS Journal of Photogrammetry and Remote Sensing *53*, 193–203.

Lamonaca, A., Corona, P., and Barbati, A. (2008). Exploring forest structural complexity by multi-scale segmentation of VHR imagery. Remote Sensing of Environment *112*, 2839–2849.

Lara Jr., R. D., and Mitishita, E. (2009). Automatic Digital Aerial Image Resection Controlled by LIDAR Data. In 3D Geo-Information Sciences (Berlin, Heidelberg: Springer Berlin Heidelberg), pp. 213-234. Available at: http://www.springerlink.com/index/10.1007/978-3-540-87395-2.

Leckie, D., Gougeon, F., Hill, D., Quinn, R., Armstrong, L., and Shreenan, R. (2003). Combined high-density lidar and multispectral imagery for individual tree crown analysis. Canadian Journal of Remote Sensing *29*, 633–649.

Leckie, D. G., Gougeon, F. A., Tinis, S., Nelson, T., Burnett, C. N., and Paradine, D. (2005). Automated tree recognition in old growth conifer stands with high resolution digital imagery. Remote sensing of environment *94*, 311–326.

Lee, H. S., and Younan, N. H. (2003). DTM extraction of LIDAR returns via adaptive processing. IEEE Transactions on Geoscience and Remote Sensing *41*, 2063–2069.

Lee, J. (1991). Comparison of existing methods for building triangular irregular network, models of terrain from grid digital elevation models. International Journal of Geographical Information Science *5*, 267–285.

Lefsky, M. A., Cohen, W. B., Parker, G. G., and Harding, D. J. (2002). Lidar remote sensing for ecosystem studies. BioScience *52*, 19–30.

Lim, K., Treitz, P., Wulder, M., St-Onge, B., and Flood, M. (2003). LiDAR remote sensing of forest structure. Progress in Physical Geography *27*, 88.

Liu, D., Gong, P., Kelly, M., and Guo, Q. (2006). Automatic registration of airborne images with complex local distortion. Photogrammetric Engineering and Remote Sensing *72*, 1049.

Liu, X. (2008). Airborne LiDAR for DEM generation: some critical issues. Progress in Physical Geography *32*, 31.

Maltamo, M., Mustonen, K., Hyyppä, J., Pitkänen, J., and Yu, X. (2004). The accuracy of estimating individual tree variables with airborne laser scanning in a boreal nature reserve. Canadian Journal of Forest Research *34*, 1791–1801.

Meng, X., Wang, L., Silván-Cárdenas, J. L., and Currit, N. (2009). A multi-directional ground

filtering algorithm for airborne LIDAR. ISPRS Journal of Photogrammetry and Remote Sensing *64*, 117–124.

Millar, C. I., Stephenson, N. L., and Stephens, S. L. (2007). Climate Change and Forests of the Future: Managing in the Face of Uncertainty. Ecological Applications *17*, 2145-2151.

Mitishita, E., Habib, A., Centeno, J., Machado, A., Lay, J., and Wong, C. (2008). Photogrammetric and lidar data integration using the centroid of a rectangular roof as a control point. Photogrammetric Record *23*, 19-35.

Morsdorf, F., Meier, E., Allgower, B., and Nuesch, D. (2003). Clustering in airborne laser scanning raw data for segmentation of single trees. International Archives of the Photogrammetry, Remote Sensing and Spatial Information Sciences *34*, 27–33.

Naesset, E. (2002). Predicting forest stand characteristics with airborne scanning laser using a practical two-stage procedure and field data. Remote Sensing of Environment *80*, 88–99.

Persson, A., Holmgren, J., and Söderman, U. (2002). Detecting and measuring individual trees using an airborne laser scanner. Photogrammetric Engineering and Remote Sensing *68*, 925–932.

Pitkänen, J. (2001). Individual tree detection in digital aerial images by combining locally adaptive binarization and local maxima methods. Canadian Journal of Forest Research *31*, 832–844.

Popescu, S. C., and Wynne, R. H. (2004). Seeing the trees in the forest: using lidar and multispectral data fusion with local filtering and variable window size for estimating tree height. Photogrammetric engineering and remote sensing *70*, 589–604.

Popescu, S. C., Wynne, R. H., and Nelson, R. F. (2003). Measuring individual tree crown diameter with lidar and assessing its influence on estimating forest volume and biomass. Canadian Journal of Remote Sensing *29*, 564–577.

Pouliot, D. A., and King, D. J. (2005). Approaches for optimal automated individual tree crown detection in regenerating coniferous forests. Can. J. Remote Sens *31*, 255–267.

Pouliot, D. A., King, D. J., Bell, F. W., and Pitt, D. G. (2002). Automated tree crown detection and delineation in high-resolution digital camera imagery of coniferous forest regeneration. Remote Sensing of Environment *82*, 322–334.

Power, M. E., Rainey, W. E., Parker, M. S., Sabo, J. L., Smyth, A., Khandwala, S., Finlay, J. C., McNeely, F. C., Marsee, K., and Anderson, C. (2004). River-to-watershed subsidies in an old-growth conifer forest. Food webs at the landscape level, 217–240.

Refaeilzadeh, P., and Tang, L. (2009). Cross-Validation. In Encyclopedia of Database Systems, L. Liu and M. Tamer, eds. (Boston, MA: Springer US). Available at:

http://www.springerlink.com/index/10.1007/978-0-387-39940-9.

Reutebuch, S. E., Andersen, H. E., and McGaughey, R. J. (2005). Light detection and ranging (LIDAR): an emerging tool for multiple resource inventory. Journal of Forestry *103*, 286–292.

Reutebuch, S. E., McGaughey, R. J., Andersen, H. E., and Carson, W. W. (2003). Accuracy of a high-resolution lidar terrain model under a conifer forest canopy. Canadian Journal of Remote Sensing *29*, 527–535.

Schenk, T., and Csathó, B. (2002). Fusion of lidar data and aerial imagery for a more complete surface description. International Archives of Photogrammetry Remote Sensing and Spatial Information Sciences *34*, 310-317.

Silvan-Cardenas, J. L., and Wang, L. (2006). A multi-resolution approach for filtering LiDAR altimetry data. ISPRS journal of photogrammetry and remote sensing *61*, 11–22.

Sithole, G., and Vosselman, G. (2004). Experimental comparison of filter algorithms for bare-Earth extraction from airborne laser scanning point clouds. ISPRS Journal of Photogrammetry and Remote Sensing *59*, 85–101.

Sithole, G., and Vosselman, G. (2001). Filtering of laser altimetry data using a slope adaptive filter. International Archives of Photogrammetry Remote Sensing and Spatial Information Sciences *34*, 203–210.

Sohn, G., and Dowman, I. J. (2008). A model-based approach for reconstructing a terrain surface from airborne LIDAR data. The Photogrammetric Record *23*, 170–193.

Soille, P. (2003). Morphological image analysis : principles and applications 2nd ed. (Berlin ;;New York: Springer).

Solberg, S., Naesset, E., and Bollandsas, O. M. (2006). Single tree segmentation using airborne laser scanner data in a structurally heterogeneous spruce forest. Photogrammetric engineering and remote sensing *72*, 1369.

Stone, M. (1974). Cross-validatory choice and assessment of statistical predictions. Journal of the Royal Statistical Society. Series B (Methodological), 111–147.

Strahler, A. H., Woodcock, C. E., and Smith, J. A. (1986). On the nature of models in remote sensing. Remote Sensing of Environment *20*, 121–139.

Straub, B., and Heipke, C. (2007). Automatic extraction and delineation of single trees from remote sensing data. Machine Vision and Applications *18*, 317-330.

Suarez, P., Anderson, W., Mahal, V., and Lakshmanan, T. R. (2005). Impacts of flooding and climate change on urban transportation: a systemwide performance assessment of the

Boston Metro Area. Transportation Research Part D *10*, 231–244.

UC Natural Reserve System (2010). Angelo Coast Range Reserve. Angelo Coast Range Reserve. Available at: http://nrs.ucop.edu/Angelo.htm [Accessed May 30, 2010].

Vega, C., and St-Onge, B. (2008). Height growth reconstruction of a boreal forest canopy over a period of 58 years using a combination of photogrammetric and lidar models. Remote Sensing of Environment *112*, 1784-1794.

Vincent, L. (1993). Morphological grayscale reconstruction in image analysis: applications and efficient algorithms. Image Processing, IEEE Transactions on *2*, 176-201.

Vosselman, G. (2000). Slope based filtering of laser altimetry data. International Archives of Photogrammetry and Remote Sensing *33*, 935–942.

Wack, R., Schardt, M., Lohr, U., Barrucho, L., and Oliveira, T. (2003). Forest inventory for eucalyptus plantations based on airborne laserscanner data. The International Archives of the Photogrammetry, Remote Sensing and Spatial Information Sciences.

Wack, R., and Wimmer, A. (2002). Digital terrain models from airborne laserscanner data-a grid based approach. International Archives of Photogrammetry Remote Sensing and Spatial Information Sciences *34*, 293–296.

Wang, L. (2003). Object-based methods for individual tree identification and tree species classification from high-spatial resolution imagery.

Wang, L., Gong, P., and Biging, G. S. (2004). Individual tree-crown delineation and treetop detection in high-spatial-resolution aerial imagery. Photogrammetric engineering and remote sensing *70*, 351–357.

Wang, Y., Weinacker, H., and Koch, B. (2007). Development of a Procedure for Vertical Structure Analysis and 3D Single Tree Extraction within Forests Based on Lidar Point Cloud. International Archives of Photogrammetry, Remote Sensing and Spatial Information Sciences, 419–423.

Whelan, P. (2001). Machine vision algorithms in Java : techniques and implementation (London; New York: Springer).

Wolf, P., and Dewitt, B. A. (2000). Elements of photogrammetry : with applications in GIS. 3rd ed. (Boston: McGraw-Hill).

Wulder, M. (2000). Local Maximum Filtering for the Extraction of Tree Locations and Basal Area from High Spatial Resolution Imagery. Remote Sensing of Environment *73*, 103-114.

Wulder, M., Bater, C., Coops, N., Hilker, T., and White, J. (2008). The role of LiDAR in

sustainable forest management. FORESTRY CHRONICLE *84*, 807-826.

Wulder, M. (2003). Remote sensing of forest environments : concepts and case studies (Boston: Kluwer Academic Publishers).

Yu, X. (2007). Methods and Techniques for Forest Change Detection and Growth Estimation Using Airborne Laser Scanning Data.

Zhang, K., Chen, S. C., Whitman, D., Shyu, M. L., Yan, J., Zhang, C., and others (2003). A progressive morphological filter for removing nonground measurements from airborne LIDAR data. IEEE Transactions on Geoscience and Remote Sensing *41*, 872–882.

Zitova, B., and Flusser, J. (2003). Image registration methods: a survey. Image and vision computing *21*, 977–1000.